UNIVERSITY OF SÃO PAULO
SÃO CARLOS SCHOOL OF ENGINEERING

ANGELO FERNANDES ANDREOLI

Resistance upset welding of Zr-based bulk metallic glasses

Soldagem por Resistência de topo de vidros metálicos maciços de base Zr

São Carlos
2017

ANGELO FERNANDES ANDREOLI

Resistance upset welding of Zr-based bulk metallic glasses

Original Version

Thesis presented to the Materials Science and Engineering Program of the University of São Paulo to obtain the title of Master of Science

Concentration Area: Development, Characterization, and Application of Materials

Supervisor: Prof. Dr. Marcelo Falcão de Oliveira

São Carlos

2017

Andreoli, Angelo Fernandes
A555r Resistance upset welding of Zr-based bulk metallic glasses / Angelo Fernandes Andreoli; orientador Marcelo Falcão de Oliveira. São Carlos, 2017.

Dissertação (Mestrado) - Programa de Pós-Graduação em Ciência e Engenharia de Materiais e Área de Concentração em Desenvolvimento, Caracterização e Aplicação de Materiais -- Escola de Engenharia de São Carlos da Universidade de São Paulo, 2017.

1. bulk metallic glass. 2. amorphous metal. 3. crystallization. 4. welding. 5. resistance upset welding. I. Título.

FOLHA DE JULGAMENTO

Candidato: Tecnólogo **ANGELO FERNANDES ANDREOLI.**

Título da dissertação: "Soldagem por resistência de topo de vidros metálicos maciços de base Zr".

Data da defesa: 18.12.2017.

Comissão Julgadora:	**Resultado:**
Prof. Associado **Marcelo Falcão de Oliveira (Orientador)** (Escola de Engenharia de São Carlos/EESC)	Aprovado
Prof. Dr. **Claudio Shyinti Kiminami** (Universidade Federal de São Carlos/UFSCar)	Aprovado
Prof. Titular **Helio Goldenstein** (Escola Politécnica/EP-USP)	Aprovado

Coordenador do Programa de Pós-Graduação em Ciências e Engenharia de Materiais:
Prof. Associado **Antonio José Felix de Carvalho**

Presidente da Comissão de Pós-Graduação:
Prof. Associado **Luís Fernando Costa Alberto**

DEDICATION

I dedicate this thesis to my Family: my beloved Marina and my son Benício, my father Claudinei, my mother Samira, and my siblings Samir and Claudine.

ACKNOWLEDGEMENTS

To my sweetheart Marina Gamito and our beloved son Benício who was born during this period. They demonstrated all their love, support, and patience since the beginning of my master's course. All my love!

To my parents Claudinei and Samira who have provided me through moral and emotional support in my life and invested all their efforts for my education! I am eternally grateful.

To my siblings Samir and Claudine for all their support and to know I can always count on them!

I would like to express my gratitude to my supervisor Dr. Marcelo Falcão de Oliveira for his valuable advices and for conducting the supervision of my thesis with great dedication.

With a special mention to all my colleagues from the solidification laboratory and all the University staff from the Materials Science and Engineering Department at USP-EESC.

I would also like to thank Dr. Paulo Vilmar, Dr. Valdir Furlanetto, Dr. José Roberto Garbin and Prof. Dr. Claudio Kiminami for their assistance.

I am thankful to The São Paulo Research Foundation (FAPESP), grant number 2013/05987-8, who financed this project. I am also thankful to Coordenação de Aperfeiçoamento de Pessoal de Nível Superior (CAPES) for a scholarship support.

EPIGRAPH

“Science knows no country, because knowledge belongs to humanity and is the torch which illuminates the world. Science is the highest personification of the nation because that nation will remain the first which carries the furthest the works of thought and intelligence”.

Louis Pasteur

ABSTRACT

ANDREOLI, A. F. Resistance Upset Welding of Zr-based Bulk Metallic Glasses. 2017. 87 pp. Master Thesis – São Carlos School of Engineering, University of São Paulo, São Carlos, 2017.

Zr-based bulk metallic glasses represent an emerging important class of structural materials with interesting properties due to its amorphous nature. In this study, the structural and microstructural transformations to the heat-affected zone of a Zr-based bulk metallic glass welded by the resistance upset technology were investigated. X-ray diffraction, optical and scanning electron microscopy were used to characterize the base metal and the heat-affected zone. Vickers microhardness testing was performed to assess the mechanical response of the welded joints. The amorphous phase volume fraction measured along the welded joints shows no difference between the base metal and the heat-affected zone. It was possible to achieve a sound weld with no crystallization of the base metal by means of a proper variables setup.

Keywords: bulk metallic glass (BMG), amorphous metal, crystallization, welding, resistance upset welding.

RESUMO

ANDREOLI, A. F. Soldagem por resistência de topo de vidros metálicos maciços de base Zr. 2017. 87 f. Dissertação (Mestrado) – Escola de Engenharia de São Carlos, Universidade de São Paulo, São Carlos, 2017.

Os vidros metálicos maciços baseados em Zr representam uma importante e emergente classe de materiais estruturais com propriedades interessantes devido à sua natureza amorfa. Neste estudo, foram investigadas as transformações estruturais e microestruturais da zona termicamente afetada de um vidro metálico maciço de base Zr soldado pela processo de resistência de topo. Difração de raios-X, microscopia óptica e microscopia eletrônica de varredura foram utilizadas para caracterizar o metal base e a zona termicamente afetada. Ensaio de microdureza Vickers foi realizado para avaliar a resposta mecânica das juntas soldadas. A fração do volume da fase amorfa medida ao longo das juntas soldadas não apresentou diferença entre o metal base e a zona termicamente afetada. Foi possível obter uma solda de qualidade sem que houvesse desvitrificação do metal base através de uma combinação adequada de variáveis.

Palavras-chave: vidro metálico maciço; metal amorfo; cristalização; soldagem; soldagem por resistência de topo.

LIST OF FIGURES

LIST OF TABLES

LIST OF EQUATIONS

LIST OF ACRONYMS AND ABBREVIATIONS

AC	Alternate Current
AWS	American Welding Society
BMGs	Bulk Metallic Glasses
CAPES	Coordenação de Aperfeiçoamento do Pessoal de Nível Superior
CD	Capacitive Discharge
DC	Direct Current
DSC	Differential Scanning Calorimetry
Eq.	Equation
FAPESP	Fundação de Amparo à Pesquisa do Estado de São Paulo
GFA	Glass-Forming Ability
HAZ	Heat-Affected Zone
MFDC	Medium Frequency Direct Current
OM	Optical Microscopy
PW	Projection Welding
RMS	Root Mean Square
RSW	Resistance Spot Welding
RWMA	Resistance Welding Manufacture Alliance
SCRs	Silicon Controlled Rectifiers
SE	Secondary Electron Mode
SEM	Scanning Electron Microscopy
SW	Seam Welding
TEM	Transmission Electron Microscopy
USP	Universidade de São Paulo
UW	Resistance Upset Welding
WZ	Weld Zone
XRD	X-ray Diffraction Technique

LIST OF SYMBOLS

R_c – critical cooling rate;

T_m – melting temperature;

t_{max} – maximum sample thickness;

T_g – glass transition temperature;

T_{rg} – reduced glass transition temperature;

ΔT_x – supercooled liquid region;

T_x – crystallization temperature;

T_l – liquidus temperature;

L – liquidus phase;

α – alpha phase;

β – beta phase;

ΔG – Gibbs free energy;

T – temperature;

ΔH_f – enthalpy of fusion;

ΔS_f – entropy of fusion;

η – viscosity;

ΔT_{rg} – difference in temperature from T_m;

b – shape factor;

f – fraction of nucleus sites at the growth interface;

σ – liquid solid interface energy;

α and β – dimensionless parameters related to σ;

N_o – Avogadro number;

V – atomic volume;

R – gas constant;

E – Young's modulus

σ_{e-} yield strength;

$\sigma_{t,f}$ – tensile fracture strength;

H_v – Vickers hardness;

V_p – primary voltage;

V_s – secondary voltage;

N_p – number of windings in the primary coil;

N_s – number of windings in the secondary coil;

Φ – flux linkage;

I_p – primary current;

I_s – secondary current;

Q – heat generated;

I – electric current;

R_e – electric resistance;

t – welding time;

η – process efficiency factor;

R_b – bulk resistance;

ρ_b – material resistivity;

ρ_{RB} – material resistivity at room temperature;

Z – length of contact body;

A – contact surface;

T_{RT} – room temperature;

R_c – contact resistance;

ρ – resistivity of contact spots;

ξ – pressure factor;

H – Brinell hardness;

n – contact spot number;

F – compressive force;

R_F – film resistance;

ρ_t – tunnel resistivity;

R_T – total resistance;

T_p – peak temperature in the molten zone;

α – thermal expansion coefficient of the base metal

k – thermal conductivity of the base metal

k_e – coefficient of thermal conductivity of the electrode;

d_e – electrode diameter;

x – distance to the center of the welding nugget;

d – sample thickness;

d – interplanar distance;

Θ - diffraction angle;

λ – wavelength;

V_f – amorphous phase volume fraction;

T_p – peak temperature;

TABLE OF CONTENTS

1. INTRODUCTION

Immediately upon the isolation of Aluminum, it was a light and expensive metal, hence at that time was considered an elite material intended for ornaments and luxury items (UC RUSAL, 2016). “Aluminum began to be used in various ways at the turn of the XIX and XX centuries which created an incentive for development in a new range of industries” (UC RUSAL, 2016). It took approximately 100 years since aluminum alloys were first produced until effectively becoming a major structural engineering material. Present-day, it represents a substantial segment especially as lightweight assembly parts for the automotive and aeronautic industries. During this period, much effort was devoted into research, and funds were invested to bring to light the properties and define the potential of aluminum alloys as an engineering material.

Latest, a novel engineering class of materials has caught the attention of scientists and industrial collaborators. Bulk metallic glasses, or amorphous metals, are defined as engineering alloys that do not present long-range periodic arrangements of their atoms like conventional crystalline alloys. Due to their amorphous nature, metallic glasses show distinct mechanical and physic-chemical properties, oftentimes superior to their crystalline counterparts. These include higher elastic limit, yield strength, hardness and fracture toughness (EGAMI and IWASHITA, 2013). Low damping, high elastic energy and great wear resistance (GREER, RUTHERFORD and HUTCHINGS, 2002). They are also known for their higher resistance to corrosion (LI and ZHENG, 2016).

Bulk metallic glasses have found applications in a variety of industrial fields in the past years. Some of these include machinery structural materials (HOFFMAN et al., 2016), cutting materials, sporting goods equipment (TELFORD, 2004), medical devices and biomaterials for implants (LI and ZHENG, 2016).

One of the limitations of bulk metallic glasses is their processing route. In order to suppress the nucleation and growth of crystalline phases there is a need for considerably high cooling rates compared to conventional casting. This limits the maximum size (length or diameter) that a metallic glass can be formed. Consequently, welding and joining of these materials becomes of great concern not only for scientific advancements but for practical purposes as well.

It is well known that crystallization, structural relaxation or phase separation can lead to brittle failure in amorphous alloys (INOUE et al., 2003). Therefore, it is substantial to evaluate welding processes and parameters that favor the glassy phase and avoids devitrification. In the supercooled liquid region (ΔT_x), defined as the difference between the crystallization temperature (T_x) and the glass transition temperature (T_g), metallic glasses behave as a Newtonian fluid and can, therefore, be forged with ease. The supercooled liquid interval is the optimum temperature range for welding since no devitrification is expected for certain amount of time (KUO at al., 2010).

The resistance upset welding process (UW) combines the Joule affect and pressure to bond metallic pieces. Two types of resistances characterize this welding process, namely, contact resistance and bulk resistance. At the start of the welding process, contact resistance plays a major role but gradually it decreases and the role of the bulk resistance becomes more important. The advantages for welding metallic glasses are: (1) it is a solid-state process; (2) no filler metal is required, (3) short welding time, (4) ease of operation, (5) high cooling rates; and finally (6) low cost (KERSTENS, 2009).

The goal of this research study was to find suitable welding conditions to preserve the amorphous phase structure, avoiding crystallization, of a Zr-based bulk metallic glass after the resistance upset welding processing. Hence, preserving the advantageous mechanical and physic-chemical properties intrinsic of the amorphous phase.

2. BACKGROUND

2.1 Bulk Metallic Glasses

Latest, novel engineering metal alloys have attracted considerable attention from research groups and industrial facilities globally because of their remarkable properties. Metallic glasses, or amorphous metals, are metallic alloys with non-crystalline structures. Instead, it has a disordered structure, with atoms occupying random positions in a lack of long-range order, as can be schematically seen in Figure 2.1.

Figure 2.1 - Atomic structure of $Cu_{65}Zr_{35}$ glass, Cu atoms: red, Zr atoms: blue.

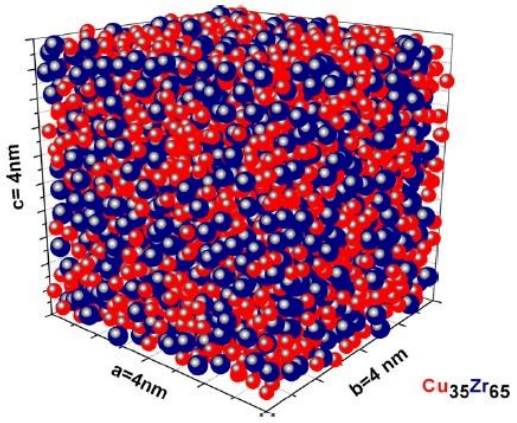

Source: Mattern et al. (2009).

This material class was first disclosed in the 60's. An $Au_{75}Si_{25}$ metallic glass alloy was synthesized from the melt at Caltech (KLEMENT; WILLENS and DUWEZ, 1960). This and other first glass-forming alloys had to be cooled extremely rapidly (about a megakelvin per second, 10^6 *K/s*) to avoid crystallization (MILLER and LIAW, 2007). The minimum cooling rate to avoid crystallization below the melting temperature (T_m) is thus defined as the critical cooling rate (R_c) for glass formation (TAKEUCHI and INOUE, 2001). An important consequence of those first metallic glasses is that they could only be produced in a limited number of forms (typically thin ribbons, sheets, or wires), (WANG, DONG and SHEK, 2004), in which the small size, in thickness or diameter, permitted the

heat to be extracted rapidly enough to reach the necessary cooling rate. Thus, samples of metallic glass (with a few exceptions) were limited to a thickness less than one hundred microns. A maximum sample thickness (t_{max}) was also defined in order to express the glass-forming ability (GFA) of such alloys (WANG, DONG and SHEK, 2004).

The work of Turnbull and Chen (1967) had an important impact to the recent born field. They showed the similarities between other non-crystalline phase materials such as polymers, ceramic glasses, and silicates with metallic glasses. They presented results showing that a second order thermodynamic transition, the glass transition (T_g), also could be observed for metallic glasses.

> Turnbull predicted that a ratio, referred to as the reduced glass transition temperature (T_{rg}) (Eq. 2.1), of the glass transition temperature (T_g) to the melting point (T_m), or liquidus temperature (T_l) of an alloy, could be used as a criterion for determining the glass-forming ability of an alloy (WANG, DONG and SHEK, 2004, p. 45).

$$T_{rg} = \frac{T_g}{T_m} \qquad \text{(Eq. 2.1)}$$

In the late 80s, the greater stabilization of the supercooled liquid started the production of the so-called bulk metallic glasses (BMGs). With thicknesses that could reach 10 mm or more, with various alloys formed from early transition metals (Zr, Ti and Hf) and production of alloys containing late transition metals (Fe-Al-Ga-P-B), due to the low production cost (MILLER and LIAW, 2007). Present-day, BMGs of the systems based on Zr, Zr–Be, Pd, Pt, Mg, La, Ni, and Cu can be formed with diameters >2 *cm*, and Fe, Co and Ti based BMG can be produced with diameters >1 *cm*, fabricated by the cooper mold casting techniques (INOUE and TAKEUCHI, 2011). Figure 2.2 presents a few of the bulk amorphous alloys developed to date. BMGs can be formed by means of vast production methods: water-quenching, copper-mold casting, high-pressure die casting, arc melting, unidirectional melting, suction casting, and squeeze casting (MILLER; LIAW, 2007). Electromechanical conformation (OLIVEIRA et al., 2002), and warm extrusion of atomized amorphous powders in the supercooled liquid region are used techniques (INOUE, 2000).

Figure 2.2 - Pd-, Ni-, Cu-, and Zr-element-based large centimeter-sized BMGs.

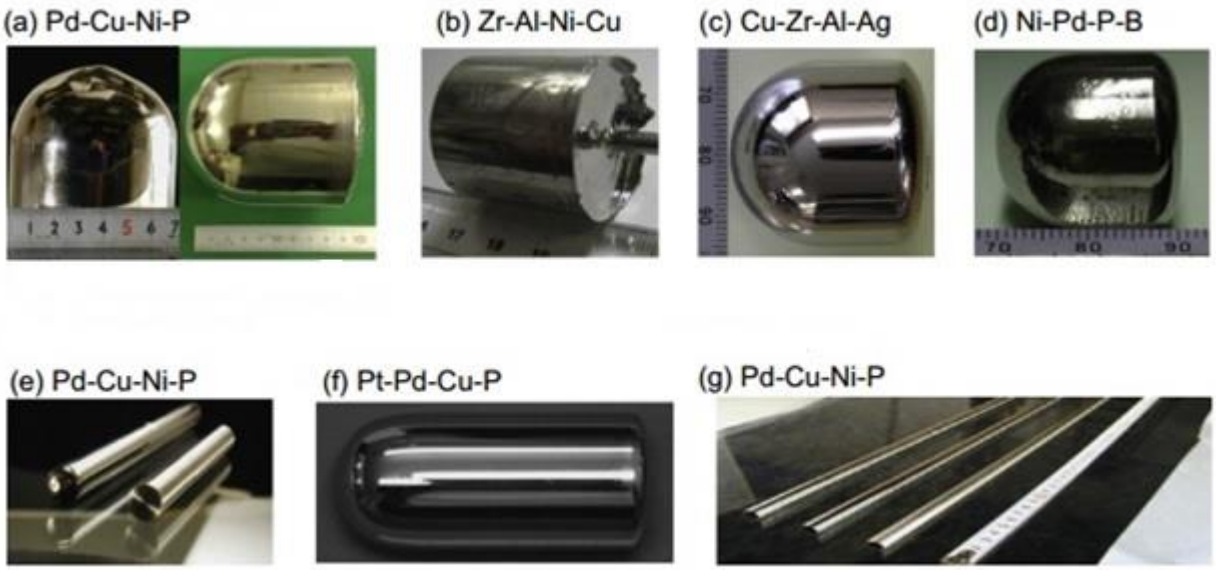

Source: Inoue and Takeuchi (2004).

BMGs present a large supercooled liquid region (ΔT_x), defined as the difference between the crystallization temperature (T_x) and the glass transition temperature (T_g) upon heating (Eq. 2.2).

$$\Delta T_x = T_x - T_g \qquad \text{(Eq. 2.2)}$$

Figure 2.3(a) demonstrates the interdependence between the reduced glass transition temperature (T_{rg}), critical cooling rate (R_c) and maximum sample thickness (t_{max}) for a variety of glassy alloy classes. Figure 2.3(b) shows the relation between the temperature interval of the supercooled liquid region, critical cooling rate (R_c), and maximum sample thickness (t_{max}). It can be inferred from Figure 2.3 that with the increase in (T_{rg}), there is a clear tendency for lower critical cooling rates and sizable samples. Likewise, the increase in ($\Delta T_{x)}$ leads to reduced cooling rates and thicker samples (t_{max}). A linear correlation between these parameters is shown in both cases. The multicomponent BMGs have deep eutectic valleys leading to the appearance of high T_{rg} and large $\Delta T_{x.}$ “Designing the alloy

choosing an alloy composition exhibiting a lower liquidus temperature near the eutectic point is an effective way of finding an appropriate BMG composition" (INOUE and TAKEUCHI, 2011, p. 2246). This is visually described in Figure 2.4.

Figure 2.3 – a) Correlation between (T_{rg}), (R_c) and (t_{max}) for bulk glassy alloys b) Relationship between (R_c), (t_{max}), and (ΔT_x) for BMGs.

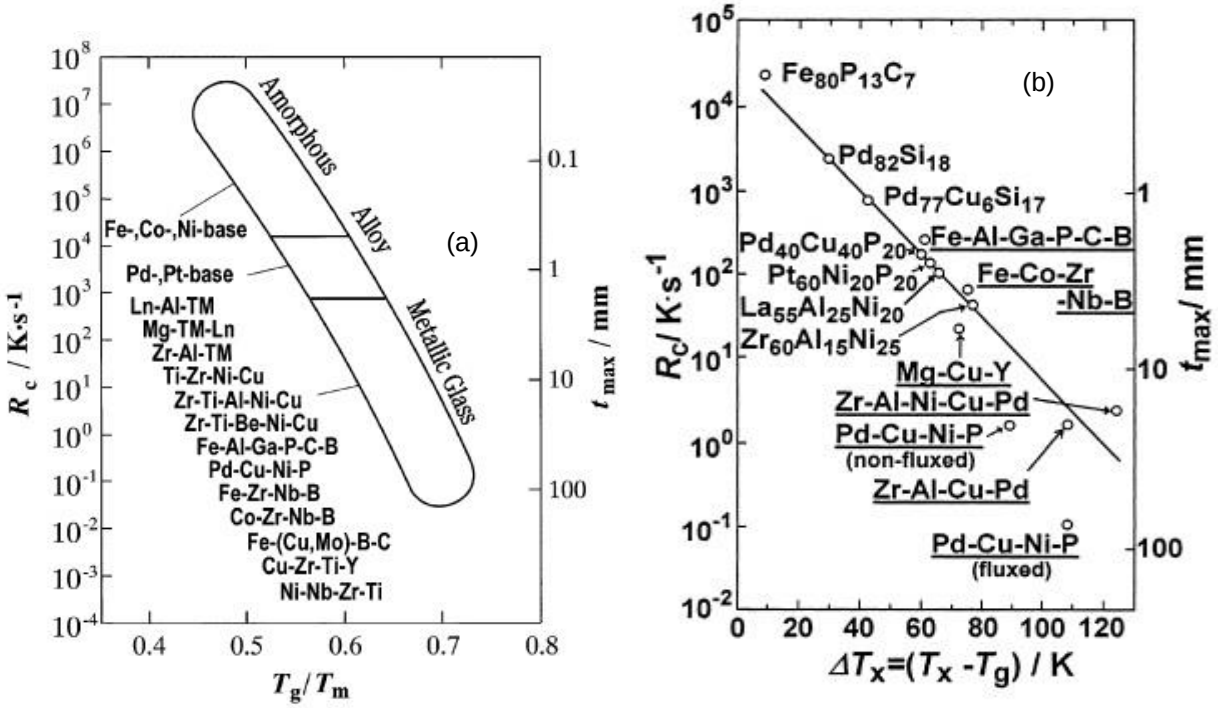

Source: Inoue (2000).

Figure 2.4 - Schematic variation of the glass transition temperature, T_g, liquidus temperature, T_l, the reduced glass transition temperature, T_{rg}, in two different types of eutectic systems—deep eutectic and shallow eutectic.

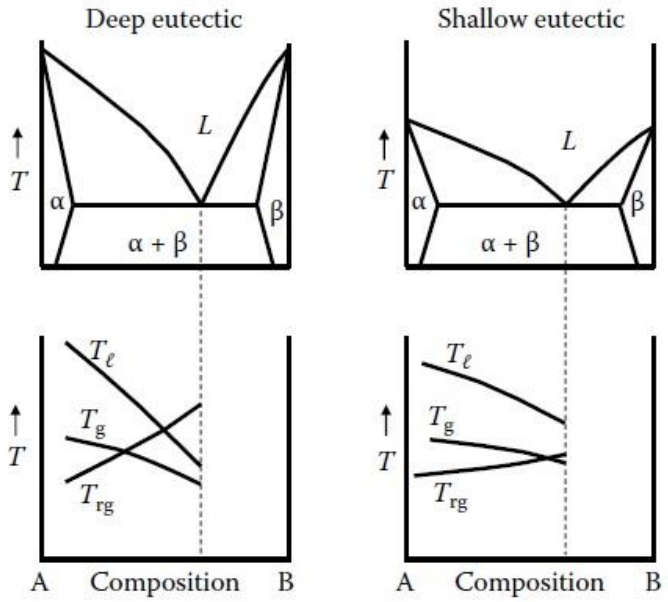

Source: Suryanarayana and Inoue (2010).

2.1.1 Thermodynamics, Kinetics, and Structure Models

Inoue (1995), regarding the GFA of BMGs stated three empirical rules: (1) the multicomponent system should consist of three or more elements, (2) there should be a significant difference (greater than 12*%)* in the atomic sizes of the main constituent elements, and (3) the main elements should have negative heats of mixing. Inoue et al. (2002) reported that the atomic size mismatch rather than the negative heat of mixing between the constituent elements dominate the stabilization of the supercooled liquid.

Understanding the kinetics and thermodynamics of undercooled liquids is essential to comprehend the glass-forming ability of BMGs. Large GFA are achieved when the free energy is low for the transformation of liquid to crystalline phases. Since Gibbs free energy is expressed as:

$$\Delta G = \Delta H_f - T\Delta S_f \qquad \text{(Eq. 2.3)}$$

Where;

ΔG is Gibbs free energy

T is temperature

ΔH_f is the enthalpy of fusion;

ΔS_f is the entropy of fusion.

Low values of ΔG are obtained when the enthalpy of fusion is low and the entropy of fusion is large (Inoue, 1995). ΔS_f is expected to increase with the increase in the number of elements that constitute the system, seeing that the entropy of fusion is reciprocal to the number of microscopic states (Inoue, 1995). High reduced glass transition temperature, large interface energy between liquid/solid phases, and low enthalpy of fusion causes low chemical potential, which also leads to low ΔG at constant temperatures. Based on this thermodinamical conditions, Inoue (1995) concludes that the increment in the number of components leading to increased ΔS_f causes the increase in the degree of dense random packing which favors the decrease of ΔH_f and increase in the solid/liquid interfacial energy.

When the temperature of a molten metal is reduced below the liquidus temperature (T_l), the Gibbs free energy of the supercooled liquid is higher than that of the competing crystal(s), and the difference (ΔG), is the driving force towards crystallization (SURYANARAYANA and INOUE, 2010). “An activation energy barrier needs to be overcome before solid nuclei could form in the melt, and this activation barrier is smaller the larger the liquid undercooling is” (SURYANARAYANA and INOUE, 2010, p. 16). Considering that the nucleation rate of a crystalline phase (I), and the crystal growth rate (U) are expressed as (Inoue, 1995):

$$I = \frac{10^{30}}{\eta} * exp\left[\frac{-b\alpha^3\beta}{T_{rg}\left(1-T_{rg}\right)^2}\right][cm^{-3}s^{-1}] \qquad \text{(Eq. 2.4)}$$

$$U = \frac{10^2 f}{\eta} * \left[1 - exp\left(-\beta \Delta T_{rg}/T_{rg}\left(\frac{T}{T_m}\right)\right)\right][cms^{-1}] \qquad \text{(Eq. 2.5)}$$

Where;

η is the viscosity;

T_m is the melting temperature;

ΔT_{rg} is the difference in temperature from T_m;

b is a shape factor and 16π/3 for spherical nucleus;

f is the fraction of nucleus sites at the growth interface;

α and β are dimensionless parameters related to liquid/solid interface energy (σ);

Inoue (1995) states that (ΔS_f) and (ΔH_f) can be expressed in terms of α and β, where N_o is the Avogadro number, V atomic volume, and R the gas constant:

$$\alpha = \frac{(N_o V)^{1/3}\sigma}{\Delta H_f} \qquad \text{(Eq. 2.6)}$$

$$\beta = \frac{\Delta S_f}{R} \qquad \text{(Eq. 2.7)}$$

The main parameters to be considered in these equations are η, α, and β. “The increase in the three parameters causes the decrease in I and U values, leading to the increase in glass-forming ability” (INOUE, 1995, p.867).

For BMGs, a large undercooling gradient can be achieved due to the high cooling rates that overlaps heterogeneous crystal nucleation. The viscosity of the supercooled liquid increases dramatically as the temperature decreases and at a determined

temperature the viscosity is so high that the structure ‘freezes’ into a glassy state (SURYANARAYANA and INOUE, 2010). The temperature interval where this phenomenon occurs is the glass transition temperature. Viscosity indicates the resistance to flow of a system and is a measure of its internal friction. The International System unit for viscosity is $Pa.s = kg\ m^{-1}\ s^{-1}$.

One mechanism that was determined to be the reason for the stabilization of a BMG in an amorphous phase is the necessity for long-range atomic configurations to construct the crystalline phase with a large volume unit cell from the glassy structure. This phenomenon causes the retardation of the crystalline reaction (INOUE; TAKEUCHI, 2002). This feature of the atomic configuration leads to the formation of high degree of dense random packing for the amorphous phase and was demonstrated by the small difference in densities between amorphous alloys and their crystalline counterparts (INOUE and TAKEUCHI, 2002). The smaller difference in densities also suggests that the release of free volume during the transformation of the supercooled liquid to crystal is lower than that of ordinary crystallizations with larger density differences. The less the free volume in the structure the less the mobility of atoms, which difficult crystallization (PEREIRA, 2009). Bulk metallic glasses satisfy the three empirical rules leading to a high interfacial energy between the liquid/solid phases with low atomic diffusivity and the need of long-range atomic rearrangements preventing crystallization to occur (INOUE and TAKEUCHI, 2002), permitting also a high stability of the glassy phase.

2.1.2 Mechanical Properties

The high visibility that BMGs have received in recent years, both in research and development level, as for practical applications, is due to their remarkable mechanical, thermomechanical, physiochemical, and soft magnetic properties. The possibility to make use of such features in structural engineering, such as biocompatible prostheses (QIN et al., 2011), sporting equipments (TELFORD, 2004), super-precision microgears (ISHIDA et al., 2007), and magnetic shielding (ASHBY and GREER, 2006), to cite a few, are attractive for further technological and scientific research. Despite metallic glasses were first developed in the 60’s, studies of mechanical properties began in the 70’s. Egami,

Iwashita and Dmowski (2013), did an extensive review on the mechanical properties of bulk glassy metals and concluded that, in a first instance, these do not seem to reflect the disordered atomic nature of BMGs, being superficially equal to the crystalline materials. However, on a deeper view they recognize that the amorphous structure has deep and intrinsic effect on the mechanical properties.

When comparing the mechanical strength and elastic limit of Zr-based BMGs with crystalline steels and Ti alloys BMGs present compatible densities, but lower Young's modulus (96 *GPa*) and higher elastic limit deformation until fracture (2*%)* (TELFORD, 2004). They have high yield strength (σ_e = 1.9 GPa) and high resistance per unit volume, making them candidates for replacing aluminum in the sports industry applications (TELFORD, 2004). Figure 2.5 shows a comparative diagram of the tensile strength and Vickers's hardness with Young's modulus of various engineering materials.

Figure 2.5 – The relations between mechanical properties of typical BMGs: (a) tensile fracture strength ($\sigma_{t,f}$) with Young's modulus (E); (b) Vickers hardness (Hv) with Young's modulus (E).

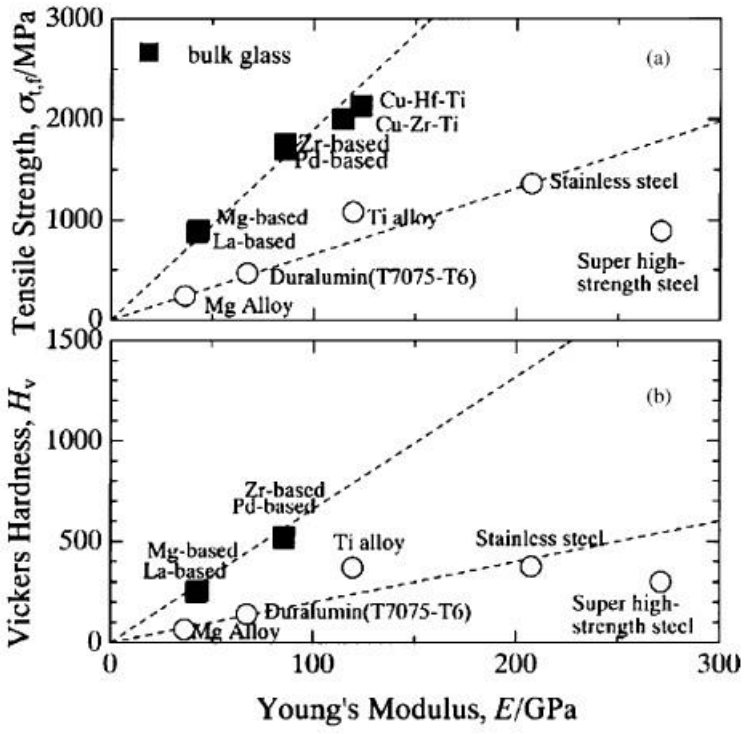

Source: Wang, Dong and Shek (2004).

In Fig. 2.5, it is clear to see the advantageous mechanical features of BMGs when correlated to traditional crystalline alloys. The deformation and fracture mechanisms is believed to reflect the significant difference of the mechanical properties between BMGs and crystalline alloys. “Plastic deformation in metallic glasses is generally associated with inhomogeneous flow in highly localized shear bands” (WANG, DONG and SHEK, 2004, p. 69). At higher temperatures and lower stress, the flow is homogeneous and essentially Newtonian viscous.

Zhang and Inoue (2002) reported the development of a Ni-based BMG prepared by mold-clamp and cooper mold casting methods with a tensile fracture strength of 2.7 *GPa*, tensile fracture elongation of 2.1*%,* compressive fracture strength of 3.01 *GPa* and compressive fracture elongation of 2.4*%.* The $Co_{43}Fe_{20}Ta_{5.5}B_{31.5}$ glassy alloy shows the higher strength known to date for a BMG and it exceeds 5 GPa (INOUE et al., 2003). BMGs also exhibit great wear resistance properties (GREER; RUTHERFORD and HUTCHINGS, 2002). Metallic glasses also have some outstanding properties, including uniquely high capacity for elastic energy storage per unit volume or mass, low damping; in some cases, very high toughness (ASHBY and GREER, 2006), and good corrosion resistance (MILLER and LIAW, 2007). The best combination of toughness and strength known up to date belongs to a $Pd_{79}Ag_{3.5}P_6Si_{9.5}Ge_2$ metallic alloy (DEMETRIOU et al., 2011).

However, BMGs are generally brittle and present poor or none plasticity at room temperature (JOHNSON, 1999). Despite Zr-based and Pd-based BMGs show some plasticity, this is constrained to localized shear bands, thus, they cannot be considered ductile. The fracture surface of these alloys present a typical vein pattern and high local plasticity arising from instabilities in the band of lowered viscosity (LEWANDOWSKI, WANG and GREER, 2005), shown in Figure 2.6. Latest research has shown that the Poisson’s ratio of BMGs has a direct relationship to mechanical properties such as shear modulus and fracture energy (GU et al., 2008). Du et al. (2009) reported that by varying the composition of a class of Fe-BMGs, a well-defined transition from brittleness to plasticity was observed as the Poisson’s ratio rose above the critical value of 0.32. One of the challenges to establish BMGs as structural materials is the need for alloys designed with improved plasticity at room temperature.

Figure 2.6 - Scanning electron micrograph (SEM) of the fracture surface of $Zr_{41}Ti_{14}Cu_{12.5}Ni_{10}Be_{22.5}$ BMG (scale markers: 5 μm).

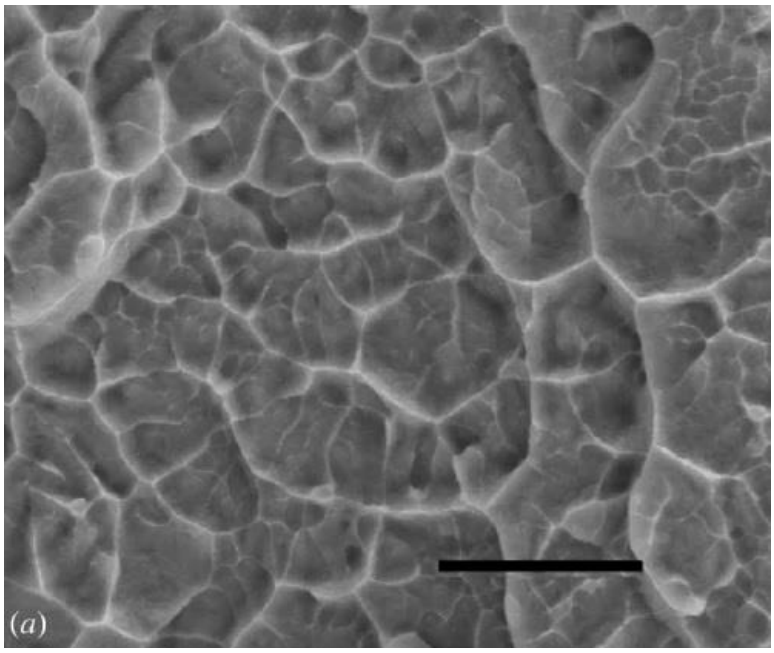

Source: Lewandowski, Wang and Greer (2005).

2.1.3 Supercooled Liquid and Superplasticity

The deformation behavior of metallic glasses is separated in two different stages. Below the glass transition, they reveal an inhomogeneous deformation, which leads to the appearance of discrete and thin shear bands, resulting of its non-hardenable nature (KAWAMURA et al., 1997). However, in the supercooled liquid region, (ΔT), BMGs usually exhibit a drastic reduction of viscosity, and therefore, present a Newtonian flow behavior (WANG et al., 2005), and can retain its amorphous structure even after large plastic deformation (KIM, MA, and JEONG, 2003).

Kawamura et al. (1997) studied superplasticity of a bulk $Zr_{65}Al_{10}Ni_{10}Cu_{15}$ glassy alloy ribbon in the supercooled liquid region and reported a maximum tensile elongation of 340% at an initial strain rate of 5 $x10^{-2}$ s^{-1} at 673 K. Kim, Ma and Joeng (2003) tested the same alloy, but manufactured by a different casting route. The tensile testing was conducted under a constant cross-head speed condition at 696 K in a relatively high strain rate range between 2.5$x10^{-3}$ s^{-1} and 2.5$x10^{-2}$ s^{-1}. They inform that the temperature of 696 K is the minimum viscosity to be reported. The alloy exhibited a tensile elongation as large

as 750% at 6.3 x 10^{-3} s^{-1}–696 K though crystallization occurred during deformation. Figure 2.7 shows the stress-strain curves of $Zr_{65}Al_{10}Ni_{10}Cu_{15}$ BMG at different temperatures and strain rates.

Figure 2.7 – Stress-strain curves of $Zr_{65}Al_{10}Ni_{10}Cu_{15}$ metallic glass at various temperatures and at strain rates of 5.0 x lO^{-4} s^{-1} (a), and 5.0 x $l0^{-2}$ s^{-1} (B). The flow stress is defined as shown in the inset.

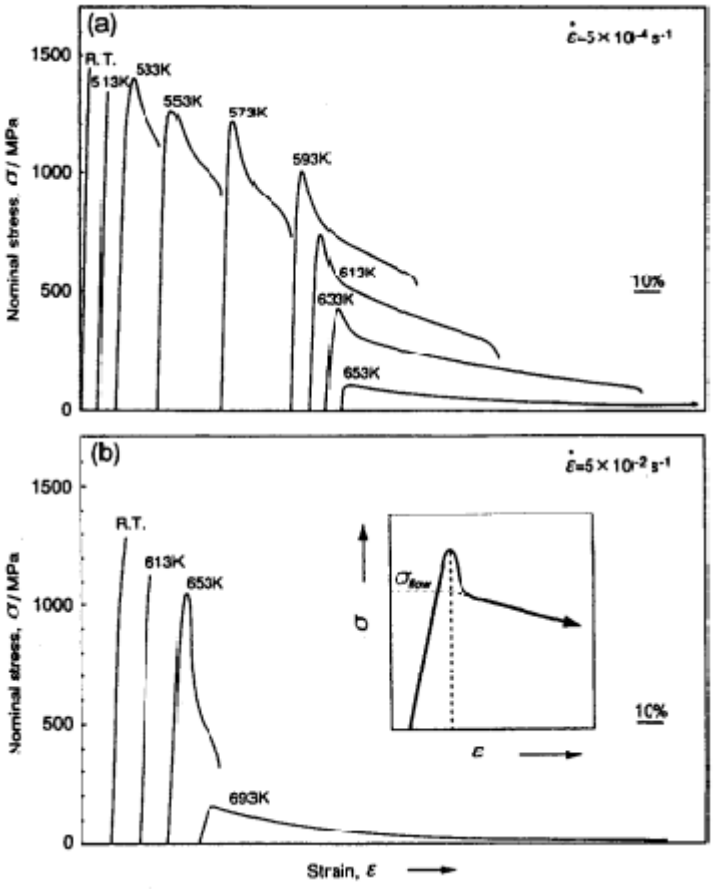

Source: Kawamura et al., (1997).

Wang et al. (2004), reported the study of a $Zr_{41.25}Ti_{13.75}Ni_{10}Cu_{12.5}Be_{22.5}$ (at. %) BMG deformation in the supercooled liquid region. The isothermal tensile results showed that at low-strain rates the material behaved like a Newtonian fluid. On the other hand, for high-strain rates the material had a non-Newtonian behavior in the initial deformation stage. The maximum elongation reached 164% at 656K. Miller and Liaw (2008) reported a tensile elongation about 20,000% for a deformed $La_{55}Al_{25}Ni_{20}$ BMG alloy in the supercooled region.

2.1.4 Present and Future Applications

The first report of a commercial use of a Zr-based BMG was the confection of golf clubs (JOHNSON, 2015). Liquidmetal Technologies Company made the first attempt to industrialize the use of this new engineering material. They were unsuccessful for two main reasons: (1) the newly developed die-casting route introduced flow lines on the surface of the part that acted like crack-initiation sites, (2) in 1997 the US Golf Association restricted the limit of how 'springy' golf clubs could be (JOHNSON, 2015). Zr-based BMGs can transfer up to 99% of the applied energy to the golf plate, whereas steel golf plates transfer 60% and titanium transfer 70% (WANG, DONG and SHEK, 2004). BMGs were also applied in other high-end sporting goods such as tennis rackets, and may find applications for baseball bats, bicycle frames, hunting bows, and skis (WANG, DONG and SHEK, 2004).

Inoue et al. (2003), informed the use of Fe-based BMGs powders as shot-peening balls. Shoot peening generates a residual compressive stress field onto the surface of metals. They reported that the residual stress caused by BMGs shot-peening balls, leading to increased hardness and resilience, is far superior to that of conventional crystalline shot-peening balls.

Present novelty and rarity make BMGs attractive for high-end lifestyle products. "The ability to take high polish and resist abrasion and corrosion suggest the use of metallic glasses for jewelry, spectacle frames, watch cases, pens, mobile-phone cases" (ASHBY and GREER, 2006, p. 326).

Ishida et al. (2007) detailed the construction of 2.4 mm Ni-based BMG microgears. It presents high durability, extraordinary dimensional as-cast stability, and wear resistance. These microgears can be used as micromotor parts for cell phones, computers, electronic and medical devices.

Li and Zheng (2016), reported of Zr-based BMGs for biomedical implants, with much higher hardness than that of conventional crystalline biomedical 316L SS, Ti alloys and Zr alloys, and high yield strength that is considerably higher than that of those above mentioned conventional crystalline metallic biomaterials. Besides the mechanical properties, alloys suitable for biomedical applications such as implants must have great

biocompatibility. Li and Zheng (2016) also showed that Zr-based BMGs presented better biocompatibility than the conventional crystalline 316L stainless steel, Zr and Zr-based alloys, as well as Ti and Ti-based alloys, for both, *in vitro* cell culture and *in vivo* rabbit implantations. Table 2.1 summarizes the potential applications of BMGs related to their intrinsic properties.

Table 2.1 – Possible application fields for BMGs (WANG, DONG and SHEK, 2004).

Properties	Application
High strength	Machinery structural materials
High hardness	Cutting materials
High fracture toughness	Die materials
High fatigue strength	Bonding materials
High corrosion resistance	Corrosion resistance materials
High elastic energy	Sporting goods materials
High wear resistance	Writing appliance materials
High reflection ratio	Optical precision materials
High hydrogen storage	Hydrogen storage materials
Good soft magnetism	Soft magnetic materials
High frequency permeability	High magnetostrictive materials
High viscous flowability	Composite materials
High acoustic attenuation	Acoustic absorption materials
Self-sharping properties	Penetrator
High wear resistance and manufacturability	Medical devices materials

2.2 Resistance Welding

The resistance welding process was invented and patented in 1885 by an American named Elihu Thompson (KERSTENS, 2009). The discovery was made during a lecture and demonstration about electricity in 1884. In response to a question from someone in the audience, Thompson created and produced an experiment that yielded the first resistance weld. It comprehends a group of welding process in which the Joule effect and pressure are used to bond metals pieces together. The four main processes

are: resistance spot welding (RSW), projection welding (PW), seam welding (SW), and resistance upset welding (UW).

2.2.1 Resistance Upset Welding

Kerstens (2009, p. 11), describes the upset welding process as:

> The two ends of a work-piece are brought together under a high welding or upsetting force before the application of the welding current. Due to the contact resistance of the two workpieces the interface becomes warmer and when the material is warm enough, an extra upsetting pressure is applied, material extrudes out-wards forming an upset, and the two workpieces join.

The literature related to this process to date has been limited (KERSTENS, 2009). Resistance upset welding, unusually of other resistance welding processes, is a solid-state welding process. It involves the interaction of electrical, thermal, mechanical and metallurgical phenomena (KERSTENS, 2009). In comparison with fusion welding processes, the metallurgical properties and chemical composition are not significantly modified leading to better mechanical properties (KANNE, 1994). Simplicity, welding speed, capability of remote control and independence of welding quality from the operator skill are the other advantages of this process (KANNE, 1994). Temperatures are lower than for fusion welding, and there are no transformations or solidification stresses induced by melting. The fact that is a solid-state process enables to weld within the supercooled liquid temperature (ΔT_x), and hence below the BMG crystallization temperature (T_x). This feature allied to short welding cycles and high cooling rates allows for the hypothesis that, with correct welding schedules, a heat-affected zone without devitrification may occur. “Because no melting is present in solid-state welds, the microstructure is very different from the solidification structures found in fusion welds. Improved properties of the weld result from the solid-state metallurgical structure” (KANNE, 1994). The distinct characterization of a welded zone (WZ) and a heat-affected zone (HAZ) cannot be done for UW. Rather, only a HAZ can be characterized and a high and low temperature zone are typical (KERSTENS, 2009). Another advantage compared to fusion processes include minor quantity of volumetric defects, such as cracks and voids.

In resistance upset welding the workpieces are not overlapped. Two parts to be joined are clamped in electrodes connected to the secondary of the resistance welding transformer (RWMA, 2003). The pieces are joined end-to-end and pressure is applied between them by the movable clamps while current flows through the electrodes. The main parameters controlled are current density, electrode force, and welding time. Figure 2.8 shows the schematic illustration of the resistance upset welding.

The UW process has been used to weld a wide range of metals including, carbon-steel, stainless steel, aluminum alloys, brass, cooper, and nickel alloys (KEARNS, 1980). As to the author's knowledge, this is the first attempt to weld BMGs by the UW process.

Figure 2.8 – a) Schematic illustration of the resistance upset welding. b) The characteristic upset flow in upset welding.

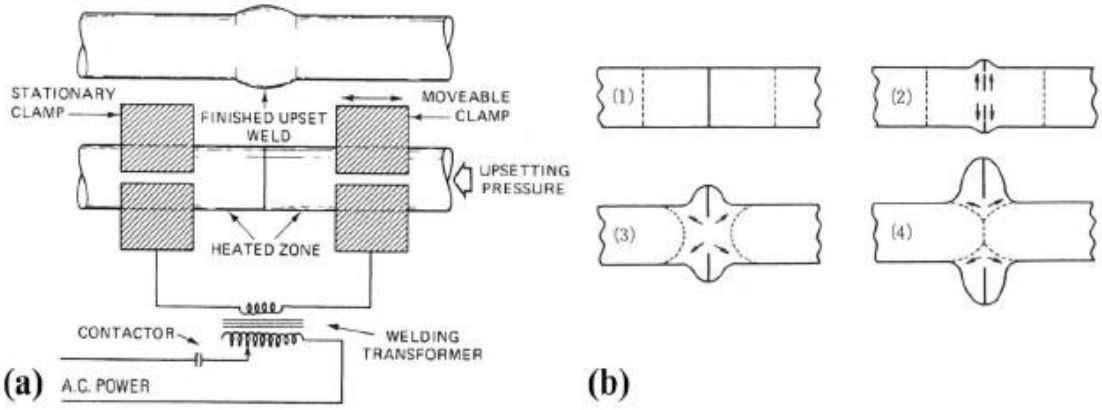

Source: Kerstens (2009).

Kearns (1980, pp. 76-77) described the essential operational steps to produce an upset welded joint as follows:

(1) Load the machine with the parts aligned end-to-end;
(2) Clamp the parts securely;
(3) Apply a welding force;
(4) Initiate the welding current;
(5) Apply an upsetting force;
(6) Cut off the welding current;
(7) Release the upsetting force;
(8) Unclamp the weldment;
(9) Return the movable platen and unload the weldment.

2.2.2 Welding Current

There are currently four main types of resistance welding power suppliers. The single-phase AC provides alternating current in the same frequency as the input power line (SALEM, 2011). The most commonly used power supply is the single-phase AC, due to its ease of use in practical applications (ZHOU and CAI, 2015). Podržaj et al. (2008) reported that this power source utilizes two silicon controlled rectifiers (SCRs) that are connected in parallel: one that passes the current during the positive half cycle and the other during the negative half cycle. Other types of power supplies are the three-phase medium frequency direct current (MFDC), the more modern capacitor discharge (CD) power supply, which provides the weld current by discharging the energy stored in a capacitor bank (SALEM, 2011). There is also the direct current (linear DC) power supply, which provides pure DC weld current through power transistors working in their linear range (SALEM, 2011).

Most resistance welding power suppliers employ an electrical transformer to convert the electrical current to the high values needed for the process to be established (BRITO, 2007). A transformer is a very simple static (or stationary) electro-magnetic passive electrical device that works on the principle of Faraday's law of induction by converting electrical energy from one value to another. Mutual induction is the process by which a coil of wire magnetically induces a voltage into another coil located near it, but electrically isolated. Figure 2.9 shows a single-phase voltage transformer construction.

Figure 2.9 – Single-phase transformer construction.

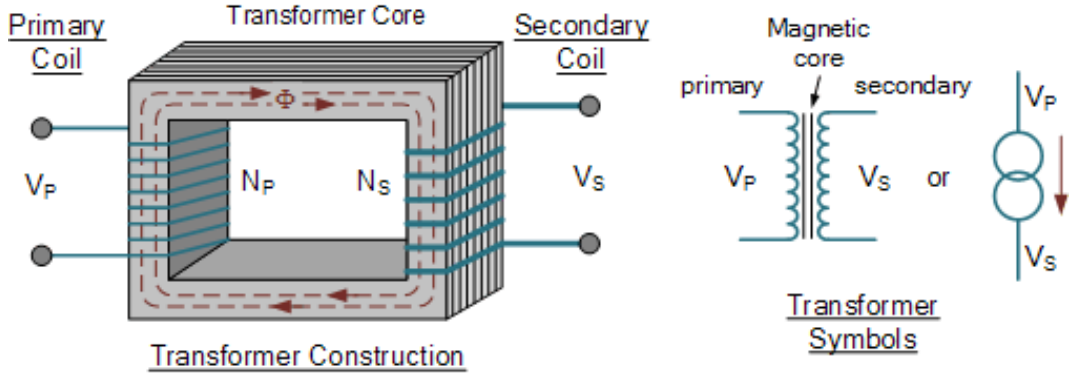

Source: EletronicTutorials (2016).

Where;

V_p- is the primary voltage;

V_s - is the secondary voltage;

N_p - is the number of windings in the primary coil;

N_s - is the number of windings in the secondary coil;

Φ - is the flux linkage.

Whenever an alternated voltage is applied to the primary coil (V_p), a voltage induction will occur in the secondary coil (V_s) by means of an electromagnetic field (Φ), analogously, currents (I_p) and (I_s) will result. In resistance welding the weld occurs in the secondary circuit of the transformer. The magnitude of voltage or current induced in the secondary coil is a function of the number of windings in each coil as formulated (BRITO, 2007):

$$\frac{I_p}{I_s} = \frac{V_p}{V_s} = \frac{N_p}{N_s} \qquad \text{(Eq. 2.8)}$$

Where;

I_p is the primary current (A)

I_s is the secondary current (A)

In electrical resistance welding the bonding occurs by heat generated by electric power sources and a force between the metals to be joined to form an electric resistance region for transient current (SENKARA and ZHANG, 2006). This process is accomplished by a short circuit of the electrical source via the weld metal to bring them to a molten state in the case of RSW, and to a relaxed solid state in UW under an applied force so that the metals will merge to form a single set. The resistance welding processes do not require filler material. The heat required to cause the metal to molten is a derivative function of the electrical resistance of metals and their contact interfaces (in micro-Ohms) divided by a variable voltage output of the electrical source to produce a welding current. The thermal energy of resistance welding process is defined by (KERSTENS, 2009):

$$Q = I^2 R_e \, t \qquad \text{(Eq. 2.9)}$$

Where;

Q is the thermal energy (J);

I is the electric current (A);

R_e is the electric resistance (Ω.m);

t is welding time (s).

2.2.3 Electrical Resistance

The electrical resistance of the upset welding process is the resistance between the electrodes. The initial value is referred as static resistance and the change with time during a welding cycle is referred to as dynamic resistance (FURLANETTO, 2010), they are both interdependent. The static resistance can be measured using an ohmmeter linked to the electrodes; it has a bulk resistance component and a contact resistance component. Bulk resistance is related to the electrical resistivity and geometry of the material being welded and usually increases with temperature (SENKARA and ZHANG, 2006). It can be calculated for upset welding using equation (2.10) (KERSTENS, 2009), where, (R_b) is bulk resistance, (ρ_b) material resistivity, (ρ_{RT}) is the material resistivity at room temperature, (Z) length of the contact body, (A) contact surface, (T) temperature, (T_{rt}) room temperature, and (α) is the coefficient of temperature dependency of the resistivity:

$$R_b = \frac{Z}{A}\rho_b(T) = \frac{Z}{A}\rho_{RT}[1 + \alpha(T - T_{RT})] \qquad \text{(Eq. 2.10)}$$

According to Umetsu et al. (2012), metallic glass (as-cast) $Zr_{55}Al_{10}Cu_{(35\ -\ x)}Ni_x$, where (x = 0, 5 or 10), shows a slight drop in resistivity with temperature increase shown

in Figure 2.10, while the crystallized alloy (after heating) will show an increase in resistivity with temperature increase.

Figure 2.10 – Electrical resistivity of Zr based BMG dependence with temperature.

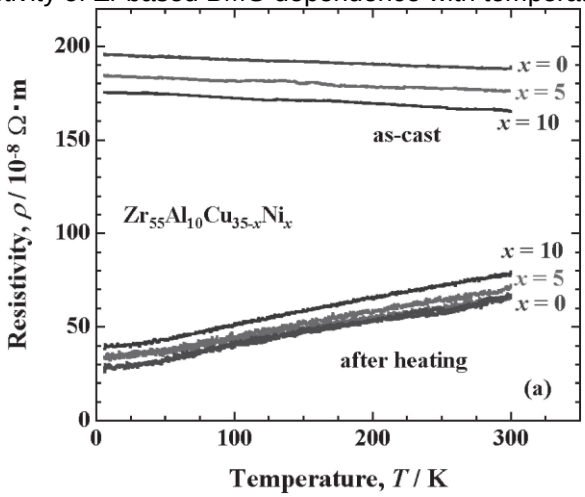

Source: Umetsu et al. (2012).

Contact resistance relates to workpiece-workpiece interface and is dependable of the welding force applied, surface conditions and temperature. “Presence of oil, oxides, dirt, scale, paints or any other foreign content causes a change in the resistance” (SENKARA and ZHANG, 2006, pp. 22). It is also very sensitive to welding pressure. The greater the welding force the higher drop of the initial contact resistance. This is due to the irregularity of the contact area of the workpieces. Only a small area is in real contact with the other workpiece due to crests and troughs at the contact interface (SENKARA and ZHANG, 2006). Consequently, lower values of resistance are expected with pressure rise since the resistivity is dependent to the workpieces contact interface by the following constriction resistance equation (Eq. 2.11), for metals with clean surfaces (TAN, 2004):

$$R_c = 0.89\rho\left(\frac{\xi H}{nF}\right)^{1/2} \qquad \text{(Eq. 2.11)}$$

Where;

R_c is the contact resistance (μΩ.m);

ρ is the resistivity of contact spots (μΩ.m);

ξ pressure factor (varies from 0.2 for surfaces with high elastic action to 1.0 for totally plastic contact);

H is the hardness (Brinell);

n is the contact spot number (totally polished surfaces tend to 1.0);

F is the compressive force (N).

Tan (2004), also describes a mathematical model for metals with a thin film or contaminants on the surface. The contact resistance is the sum of the constriction resistance and the film resistance which can be computed by equation 2.12;

$$R_F = \frac{\rho_t \xi H}{F} \qquad \text{(Eq. 2.12)}$$

Where;

R_F is the film resistance;

ρ_t is film resistance per unit area or tunnel resistivity (μΩ.m).

The total resistance (R_T) is composed by the sum of the bulk resistance and the contact resistance (constriction + film resistance) (Eq. 2.13), and changes during a welding cycle will establish the dynamic resistance of the process. The dynamic resistance can be determined dividing the instantaneous voltage by the instantaneous current.

$$R_T = R_B + R_C = R_B + (R_C + R_F) \qquad \text{(Eq. 2.13)}$$

At the beginning of the welding process, (stage I) contact resistance is dominant. As temperature increases, the breakdown of contaminants in the interface (oxides, oil, etc.), which have a higher resistivity value, and the increment of total contact area of the interface in the workpieces due to asperity softening decreases the contact resistance (stage II) and bulk resistance plays a major role (stage III) with an increment in the total resistance with temperature rise. The dynamic resistance during welding is schematically

shown in Figure 2.11. “With this method several interesting phenomena can be observed by relating the resistance variation to break-down of surface asperities, heating, melting and expulsion of various materials between electrodes” (KERSTENS, 2009).

Figure 2.11 – Theoretical dynamic resistance curve for resistance spot welding.

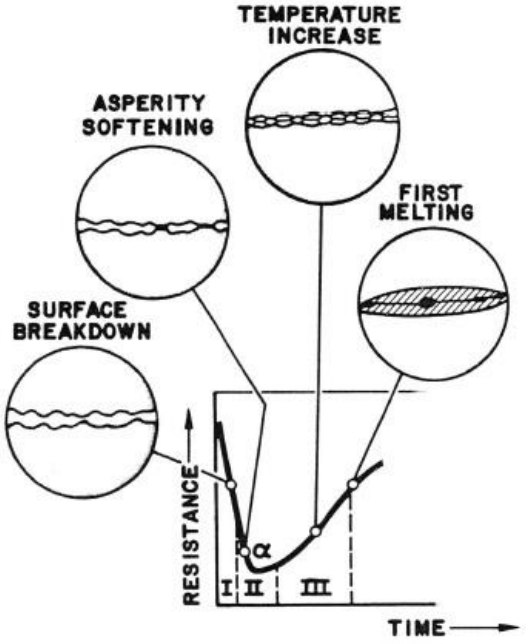

Source: Tan et al. (2004).

The resistance welding process is the sum of all the individual resistances that constitute the circuit. Figure 2.12 shows a representation of the total circuit resistance for the upset welding process. (R_E) is the electrode resistance, (R_{CE}) is the electrode-workpiece contact resistance, (R_{B1}) and (R_{B2}) are the bulk resistance of the material, and (R_C) the contact resistance at the interface.

Figure 2.12 – Schematic representation of the total resistance in upset welding.

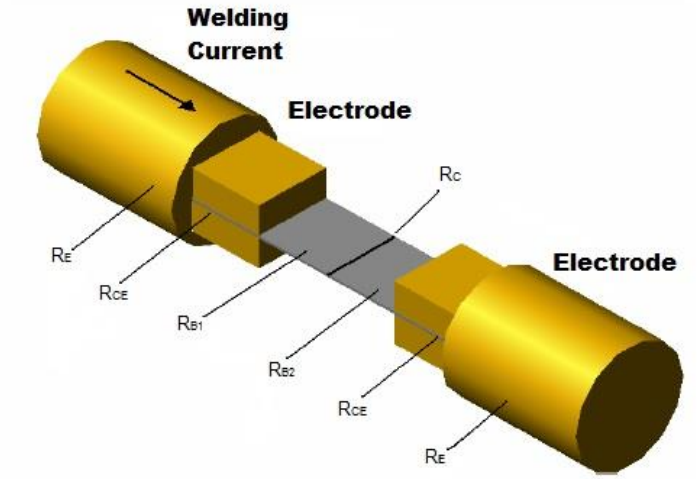

Source: adapted from Brito (2007).

2.2.4 Welding Force

As previously mentioned, the application of a welding force characterizes the resistance welding processes to join the metals parts during the process. Frequently, the welding pressure can be divided in two stages: a pre-upset force and an upset force. The pre-upset welding force is the pressure applied before the electrical current is turned on and responsible for the contact resistance between the workpieces. The pre-upset force must be lower than the material's yield strength to avoid plastic deformation (RWMA, 2003; Tang et al., 2003). The upset force is applied when current is flowing through the workpieces and heating of the interface takes place. When the material is warm enough, an extra upsetting pressure is applied, material extrudes out-wards forming an upset, and the two workpieces join. The welding force is an important parameter for resistance welding, since it directly affects the contact resistance between the materials (SONG et al., 2005). Figure 2.13 illustrates the relation between the contact resistance and welding pressure for a cooper-cooper joint.

Figure 2.13 – Resistance of the Cu/Cu joint as a function of pressure, for the joints with simply brushed surfaces, and for the joints brushed and filled with either graphite paste or conductive paste

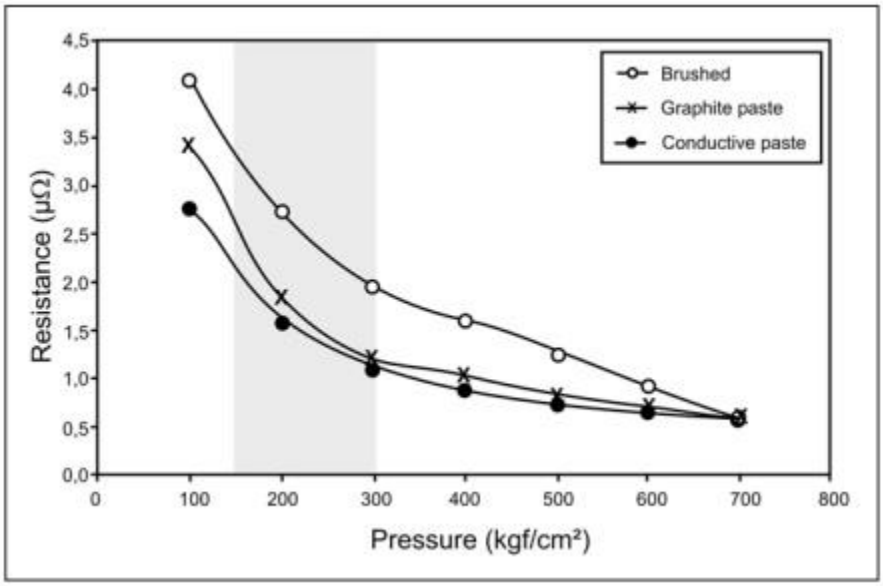

Source: Souza et al. (2006).

The welding force, usually expressed as a static value, varies dynamically during the process, and is affected by mechanical characteristics of the equipment (friction between the electrode and workpieces and inertia of the moving parts of the machine) and the electro-magnetic field formed during welding (SENKARA and ZHANG, 2006). Tang et al (2003) indicates that the welding force increases during welding due to thermal expansion experienced by the material. Figure 2.14 shows the dynamical change in welding force during the resistance welding process.

Figure 2.14 – Welding force dynamics.

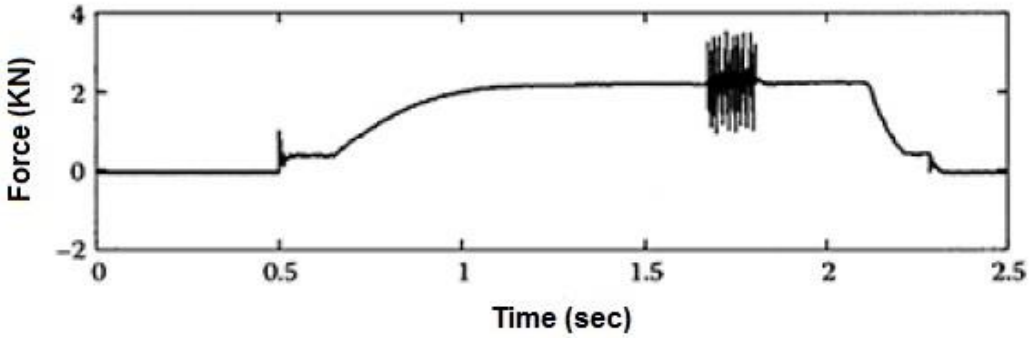

Source: Senkara and Zhang (2006).

2.2.5 Welding Time

An important parameter of the UW process is controlling the welding time. In most cases, hundreds of thousands of amperes are required for welding. Such amperage values flowing through a relatively high resistance will generate great amount of heat in a short period. To ensure good quality welds, one must have complete control over the time that the current flows between workpieces. In fact, in many welding applications, time is the only parameter that can be truly controlled. The automatic machines use electronic timers that function based on the number of AC cycles that pass through the circuit (Singh and Arora, 2013). For this reason, it is usual in the literature related to resistance welding to describe the welding time as cycles (60 *cycles* = 1 *s* for 60 Hz electric installations). If the current flow through the workpieces is constant, the amount of heat generated is proportional to the welding time, as can be inferred from equation 2.4.

2.3 Resistance Welding of Bulk Metallic Glasses

Since the development of metallic glasses, three major topics have limited its use in structural engineering: limitation of size (diameter or length), lack of workability, related to low ductility, and lack of weldability (KAWAMURA, 2004). Introduction of BMGs overcame two of the three major subjects limiting their usage, limitation of size and workability (KAWAMURA, 2004). The lack of weldability is still a topic to be studied and researched. The key objective, when studying welding of BMGs, is to determine suitable conditions, under which the joint retains the amorphous characteristic of the original material. This is important for preventing failure of the joint due to brittle fracture caused by local crystallization (WANG et al., 2014).

> It is well known that most amorphous alloys become brittle by crystallization, structural relaxation, or phase separation due to heating. Particularly, Zr-based BMGs, are easily oxidized, which leads to not only embrittlement but also an increase in the critical cooling rate required for glass formation (YOKOYAMA et al., 2002, p. 1260).

Consequently, it is difficult to weld BMGs using conventional fusion processes even in the presence of an inert gas (FUJIWARA et al., 2008; PEREIRA, 2009).

Kawamura, Kagao and Ohno (2001) were the first to disclose a successful welding of $Pd_{40}Ni_{40}P_{20}$ and $Zr_{55}Al_{10}Cu_{30}Ni_5$ alloys by friction and pulse-current methods, respectively. The welded samples were 2.5 mm in thickness, 7 mm in width, and 50 mm in length. By successful it is understood that a non-crystallized interface and heat-affected zone were achieved, as well no visible defects were observed at the interface. Figure 2.15a shows the final welded sample for the Pd-based BMG by the friction method and Figure 2.15b the final welded sample for the Zr-based BMG welded using the pulse-current process.

Figure 2.15 – External appearance of the joined BMGs

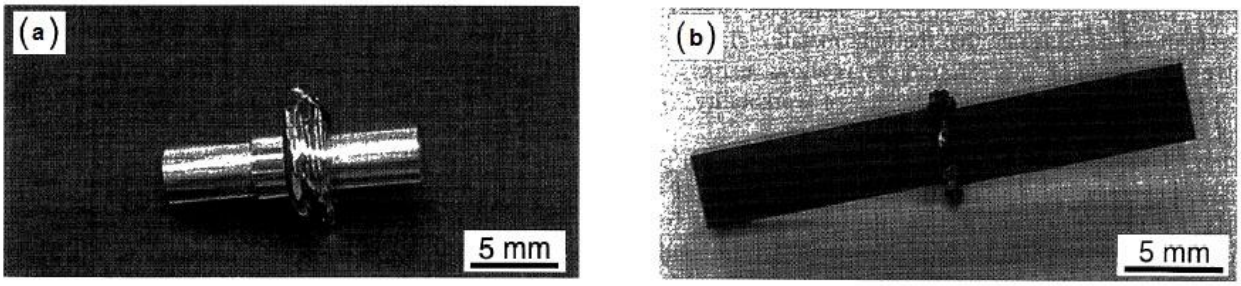

Source: Kawamura, Kagao and Ohno (2001).

Figure 2.16 shows that the micro-area X-ray diffraction confirmed a single glassy phase for both alloys, exhibiting only a halo pattern and no detectable crystalline peaks, which indicates the absence of crystalline phases. The diffraction patterns were taken from several points at the interface and heat affected zone.

Figure 2.16 – Micro-area X-ray diffraction patterns for the $Pd_{40}Ni_{40}P_{20}$ and $Zr_{55}Al_{10}Cu_{30}Ni_5$ welded samples

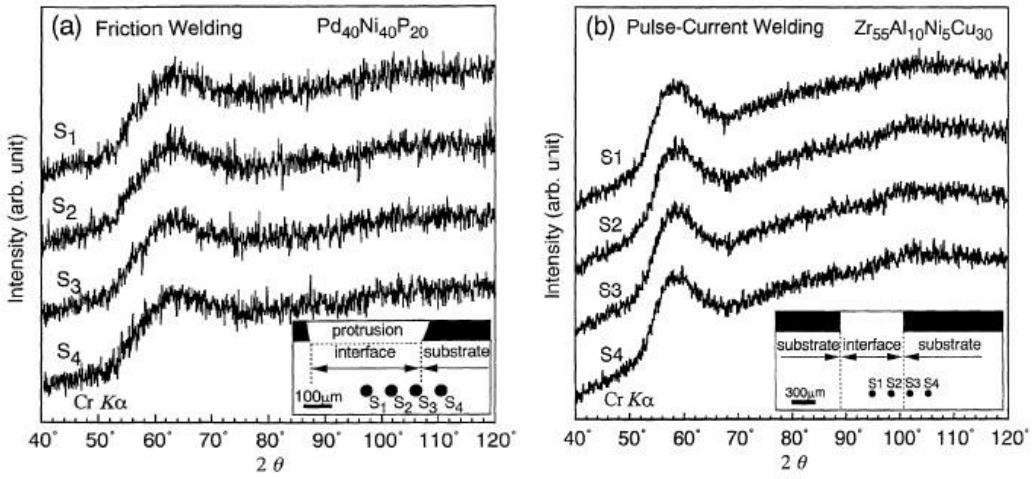

Source: Kawamura, Kagao and Ohno (2001).

Shamlaye et al. (2012), reported on resistance welding experiments using a Gleebe 350 Thermomechanical simulator. Mg-based amorphous metals were joined below the materials liquidus temperature and above the glass transition temperature. The bonding temperature of the plates was 400 °C for 0.87 seconds, and the welding pressure 245 N. Four 10 mm x 10 mm x 1 mm sheets were welded simultaneously. The results showed that it is possible to join this type of material with presence of small crystalline phases in the molten region (Figure 2.17). The Gleebe 350 can simulate a resistance upset welding process. All welding parameters (pressure, time, current, heating rate) can be precisely controlled, which is not expected when weld is made using a conventional resistance upset welder.

Figure 2.17 – Mg-based glass X-ray diffraction pattern as manufactured and after the resistance welding joining

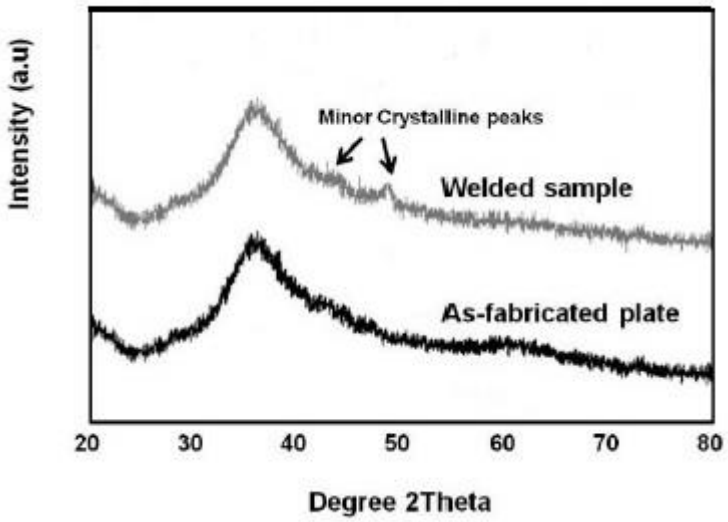

Source: Shamlaye et al. (2012).

Kuroda et al. (2009) also carried out investigation using a Gleebe Thermomechanical simulator for a $Zr_{55}Cu_{30}Al_{10}Ni_5$ alloy with 50 *μm* thickness samples. The welding schedule was done at 723 K, 20 MPa, for 5, 10, or 20 s, in a He atmosphere. With increase in welding time from 5 to 20 s, the joining efficiency increased 80%. X-ray diffraction results showed that for welding times of 5 and 10 s, no crystalline peak was detected. For the 20 s welding schedule, however, crystallization peaks for $NiZr_2$ and $Al_5Ni_3Zr_2$ were observed with halo patterns. The NiZr2 phase is the first crystallite phase to be formed during the crystallization of some Zr-based metallic glasses. “As the temperature of the metallic glass rises above the T_g, the time to crystallization is shortened. As the welding time is increased, the rate of crystallization increases” (KURODA et al., 2009). Figure 2.18 shows a transmission electron microscopy (TEM) bright-field image of the bonding interface for the Zr-based metallic glass subjected to the 20 s schedule. The nanostructures can be easily seen at the bonding interface (region A), while the base metal retained its amorphous structure (region B). The electron diffraction patterns of the selected regions A and B confirmed it (Figure 2.19).

Figure 2.18 – TEM bright-field image of the cross section at the bonding interface of the Zr-based metallic glass for the resistance welding at 723K for 20 s.

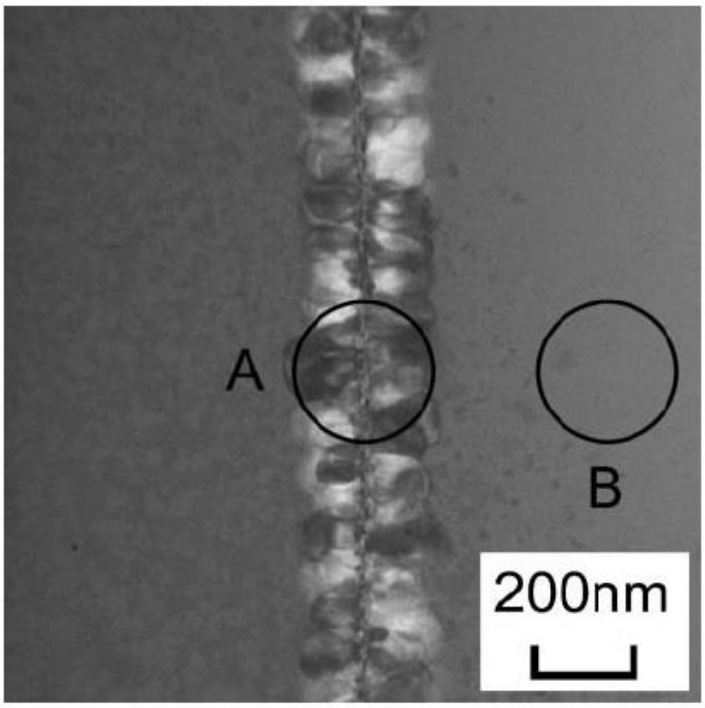

Source: Kuroda et al. (2009).

Figure 2.19 – Selected area electron diffraction patterns of mark A and mark B in Fig. 2.18 (a) Bonding interface (area A). (b) Near the interface (area B)

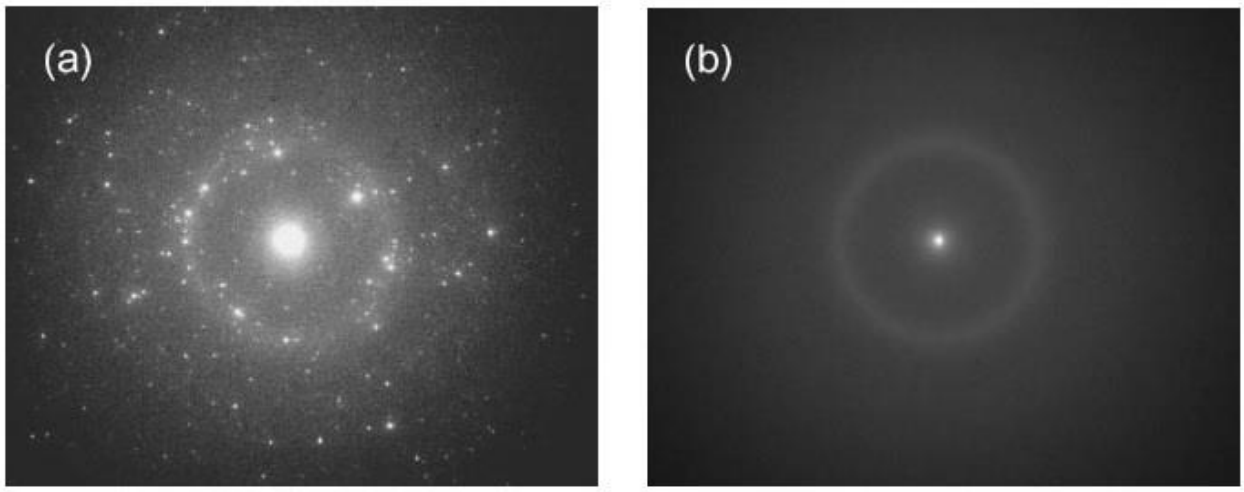

Source: Kuroda et al. (2009).

Oliveira et al. (2002) described an electromechanical process for joining metallic glasses. Pd-based BMGs were joined and showed no devitrification after bonding. A 200

A/mm^2 welding current was used and a welding force of 400 N/mm^2 applied. The methodology did not describe the welding time. The metallic glasses can deform homogeneously, like thermoplastic polymers, in the supercooled liquid region. The simultaneous application of pressure in this "superplastic" region can be used to form various parts. The electromechanical process uses this feature combined with the advantage of the high electrical resistivity of glassy metals compared to traditional metals and alloys. This resistivity is comparable to the resistivity of metals in the liquid state, in the range of 150 to 200 (Ohm.cm). The highest current density occurs at the interface between the electrode and the metal part or between the metal parts. This causes the heating to be rapid and the localized viscous flow making the conformation also rapid without undesirable crystallization or oxidation. During this process, as the deformation increases the contact interface increases by reducing the rate of heating and consequently the increase in temperature. This dynamic process is the key to achieving a low viscosity at the beginning of the process and a high viscosity at the end making the thermoconformation fast and preventing crystallization.

Johnson et al. (2012) reported on a technique for fabricating metallic structural cells used in military aircraft and space rockets, produced with a vitreous metallic matrix composite. They did not specify which class of glassy metal was used. The joining is carried out using a capacitive discharger and all contact points of the cell matrix reach temperatures of 700 °C, which is below the liquidus line and above the solidus line, in 10 milliseconds. The ductile particles dispersed in the matrix do not undergo reaction. The resulting material has a high-energy absorption capacity and does not need to be machined. They conclude that the described technique opens possibility for the manufacture of parts for the aerospace sector in large scale

Makhanlall et al. (2012), conducted experiments with resistance spot welding of glassy metals $Ti_{40}Zr_{25}Ni_3Cu_{12}Be_{20}$ and concluded that the welding current and welding time exerted a strong control over the amorphous nature of the weld nuggets produced. With increased welding energy, welding nugget and crystalline volumetric fraction tend to increase. While the nugget diameter increase makes the joint stronger, the increase in the crystalline volumetric fraction weakens the welded joint. They also conclude that with careful control of welding parameters (time and current), the crystalline volumetric fraction

of the molten region and the heat-affected zone can be reduced to a minimum. Table 2.2 shows the crystalline volume fraction of welded joints by RSW as a function of the welding parameters.

Table 2.2 - Crystalline volume fraction of welded joints as a function of welding parameters.

Time (cycle)	Current (KA)			
	5	6	7	8
2	0%	4.5%	9.2%	17.2%
3	8.4%	12.8%	14%	37.3%
4	34.1%	37.2%	57.8%	61.2%
5	56.1%	57.8%	62.1%	67.8%

Source: Makhanlall et al. (2012).

Combining the information coming from Table 2.2 and Figure 2.19, provides evidence that crystallized volume fraction is a critical parameter limiting weld spot performance in BMGs. While higher heat inputs yield bigger weld nugget diameters (Fig. 2.20) and higher tensile shear load values, the crystallized volume fraction also increases. With the increased crystalized volume fraction, there is a clear drop in shear load values. Crystallized volume fraction controls the joint mechanical response in an antagonistic fashion.

Figure 2.20 – Effects of welding parameters on joint tensile shear force and spot weld size: (a) 5 kA; (b) 6 kA; (c) 7 kA; and (d) 8 kA.

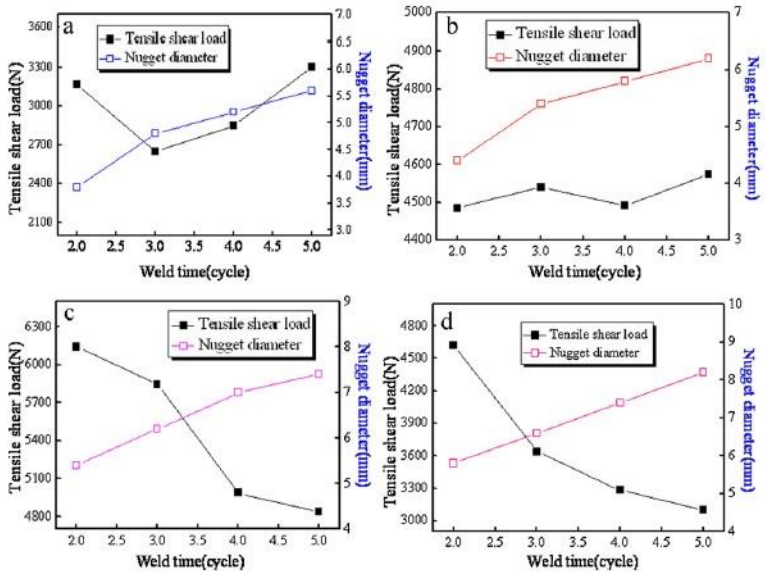

Source: Makhanlall et al. (2012).

Wang et al. (2014) carried out resistance spot welding experiments of a $Ti_{40}Zr_{25}Ni_3Cu_{12}Be_{20}$ alloy and reported that the critical cooling temperature (CCT) to achieve an amorphous microstructure in the molten zone was 1 x 10^{-3} K.s^{-1}, and that the critical temperature is the crucial factor in determining whether the welded zone will preserve the original amorphous structure. The proposed model for the CCT calculation for the RSW process is:

$$\frac{\partial T}{t} - \left(\frac{\alpha\pi^2}{4d^2}\right)\left(\frac{T}{T_p}\right)\left\{T_p - \frac{T}{1+\left(\frac{2}{\pi}\right)\left(\frac{k_e}{k}\right)\left(\frac{d}{d_e}\right)cos\left(\frac{\pi x}{2d}\right)}\right\} \qquad \text{(Eq. 2.14)}$$

Where Tp is peak temperature in the molten zone, α is the thermal expansion coefficient of the base metal, k is the thermal conductivity of the base metal, ke is the coefficient of thermal conductivity of the electrode, de the electrode diameter, x the distance to the center of the welding nugget and, t is the welding time and d the sample thickness.

3. MATERIALS AND METHODOLOGY

3.1 Samples Preparation

For the experimental part of this thesis, a Zr-based BMG was chosen. This alloy was selected due to its good GFA, with cooling rates as low as 1-100 $k.s^{-1}$, and a wide supercooled liquid region (LIU; WU and ZHANG, 2002). Zr-based BMGs also present high mechanical strength that makes them promising for structural applications (TELFORD, 2004). $Zr_{52.5}Ti_5Cu_{17.9}Al_{10}Ni_{14.6}$ (Vit 105) quinary alloys were prepared from a commercial crystalline ingot (Liquidmetal Co.) by arc melting in a purified argon atmosphere, according to Deó and Oliveira (2014). The alloy represents the nominal atomic percentage of the mixture. Bulk glassy alloy rods with 17 mm in length and 4 mm diameter were cut using a copper-diamond fast saw from the as-cast alloy rod. Transverse cross-section samples were cut from the centered region of the as-cast alloys and polished. Samples were then etched with a solution of (10% HF; 90% HNO3) 10/90 distilled water. Welded samples were longitudinally cut, polished specimens were prepared and etched with the same solution. Differential scanning calorimetry analysis (DSC), X-ray diffraction analysis (DRX), scanning electron microscopy (SEM) were used to characterize the base metal and the HAZ. The crystalline volume fraction quantification using optical microscopy images and the ZEISS AxioVs40 V4.8.2.0 software according to ASTM (2016) was performed to characterize the base metal as well as the HAZ. Vickers microhardness testing was carried out to determine the alloy hardness after welding. A thermal imaging camera was used during the welding experiments. Fig 3.1 shows the schematic illustration of the alloy synthesis facility.

Figure 3.1 – a) panoramic view of the arc-meting oven, b) base plate of the oven with the commercial alloy mixture c) cooper mold d) Zr-based BMG sample.

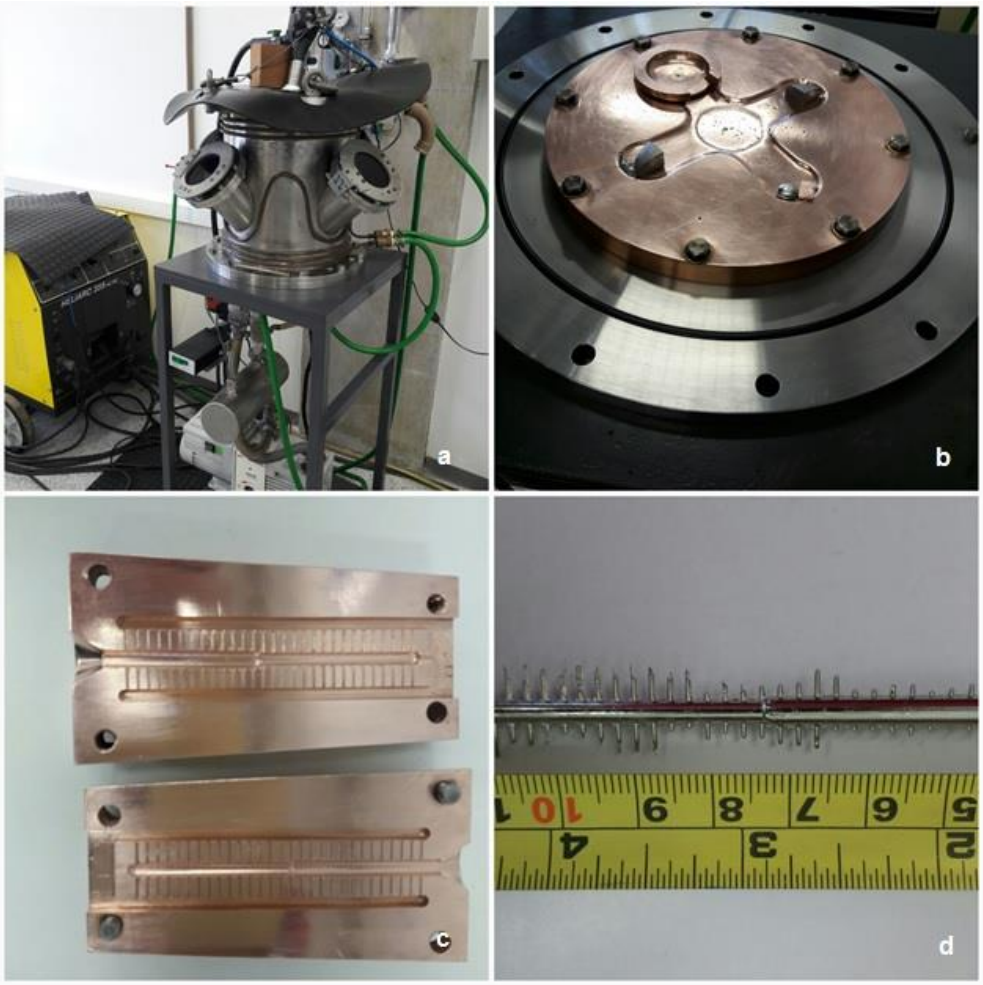

Source: Author of this thesis (2017).

3.2 Microstructural, Mechanical and Thermal Characterization

3.2.1 Differential Scanning Calorimetry

Differential scanning calorimetry is used to evaluate the thermodynamics of phase transitions that occurs to a material under a heating schedule. Transitions include first-order, and second-order. However, it does not inform into the atomic rearrangements that occur during the transition or the identity and number of the phases. A DSC measures the amount of energy absorbed, in case of endothermic transitions, or released, in the case of exothermic transitions, as it is heated, cooled, or kept at a constant temperature. Because the glass transition is a second-order transition, DSC may be used to measure

T_g, as defined by the onset of the endothermic event, as well as the onset of crystallization temperature T_x. The glass-forming ability of the BMG can be estimated directly from these parameters. In this experiment, DSC was performed for the as-cast Vit 105 alloy in the continuous heating mode. T_g, T_x, and T_l were determined using a NETZSCH DSC 404 equipment with a heating rate of 0.33 $K.s^{-1}$ up to 1000 K from room temperature. With the DSC results it was also possible to determine the ΔT_x of the amorphous alloy. Figure 3.2 shows typical differential scanning calorimetry plots for bulk metallic glasses showing T_g and T_x transitions. Table 3.1 summarizes the DSC parameters and treatment for the as-cast VIT 105 alloy.

Figure 3.2 – Typical DSC curves for bulk metallic glasses.

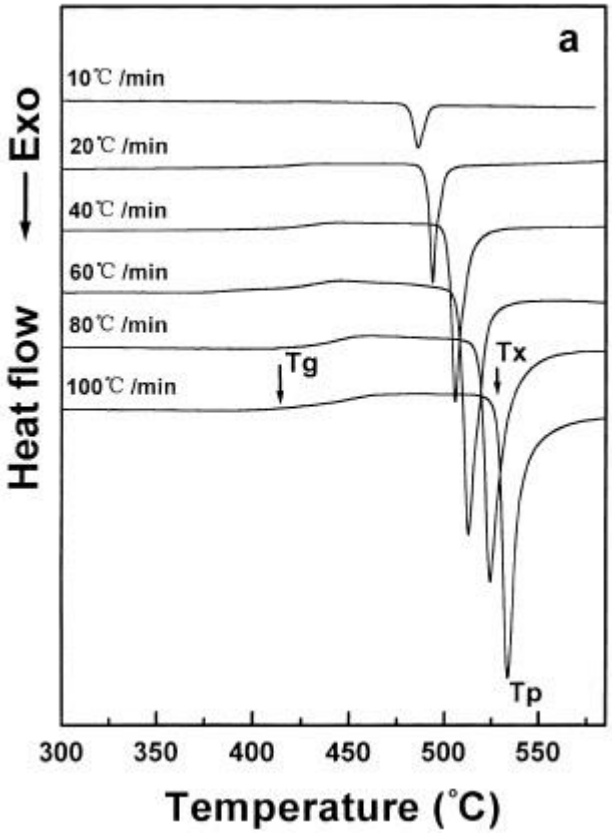

Source: LIU; WU and ZHANG (2002).

Table 3.1 – Differential Scanning Calorimetry parameters for the as-cast VIT 105 alloy.

Heating Rate (k/s)	Sample Mass (mg)	Reference	Crucible	Sample Crucible Mass (mg)	Reference Crucible Mass (mg)	Gas	Flow Rate(ml/min)
0.33	12.7	Empty	Al_2O_3	261.4	318.6	Argon	100

Source: Author of this thesis (2017).

3.2.2 X-Ray Diffraction Technique

"X-ray diffraction is frequently used to evaluate if a sample is fully amorphous from the characteristic diffuse intensity peak, and to detect and identify crystalline phases from their characteristic Bragg peaks in the diffraction patterns" (Miller and Liaw, 2008, p.121). Diffraction occurs when a wave front is scattered by a periodic array with long-range order, producing constructive interference at specific angles. The electrons in an atom coherently scatter electromagnetic radiation, hence, each atom can be considered a coherent point scatter (SPEAKMAN, 2017). The strength in which an atom scatter radiation is proportional to the number of electrons in its electron sphere. Atoms in a long-range ordered crystal are arranged in a periodic manner and thus can diffract radiation when the constructive interference of Bragg's law is met (Eq. 3.1):

$$2d\,sin\,\theta = \lambda \qquad \text{Eq. 3.1}$$

where:

d – interplanar distance;

Θ - diffraction angle;

λ – wavelength;

Hence the wavelength of X-rays is at the same scale as the interplanar distance of atoms in a crystal, it can be used to determine information about the crystal structure, including phase identification, lattice parameters, and crystallite size.

The most widely used method for producing X-rays is by causing a high-energy electron (generated at the cathode of the cathode tube) to collide with a metal target (anode) (BLEICHER and SASAKI, 2000). Figure 3.3 shows an analysis of the

phenomenon at the atomic level. When this electron reaches the target (I), an electron of the K-layer of an atom of the material is released in the form of photoelectron (II), causing a vacancy in that layer. To occupy the space left by this electron, another electron from an outermost layer passes to the K (III) layer, releasing energy in the form of an X-ray (IV) photon. The energy of this photon corresponds to the energy difference between the two layers.

Figure 3.3 – X-ray production.

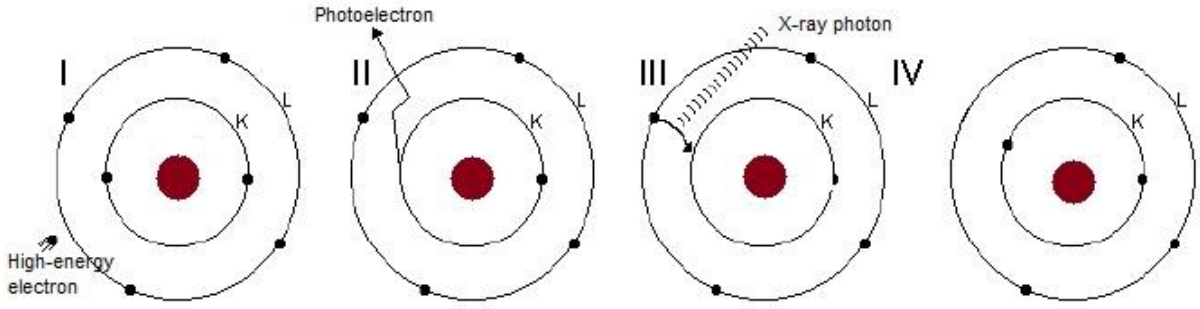

Source: Bleicher and Sasaki (2000).

X-ray diffraction technique was used to confirm the amorphous structure of the VIT 105 alloys produced for the welding procedure. After the welding procedure, transverse cross-section samples were cut from the heat-affected zone to determine whether recrystallization occurred during the welding operation. XRD was performed in the continuous scan mode, using cooper as target with a scan range from 10° to 90° *2Θ* degrees. The scan rate was 0.5° (degree/min). All XRD data were analyzed by the *X'Pert Highscore Plus* software to determine crystalline phases and/or to determine the amorphous structure of the as-cast alloys as well the welded samples.

3.2.3 Optical Microscopy

Optical microscopy (OM) is by far the most widely used technique for microstructure characterization of metals. For BMGs, OM can be used to, identify phases, quantify amorphous and crystalline volume fractions, and estimate volumetric defects, such as voids and cracks, among other utilities. One of its disadvantages is not being capable to be used in submicron scale. Therefore, light microscopy is usually done with

other complementary microstructural characterization techniques in the case of metallic glasses.

Optical microscopy allows images to be magnified through light that, after focusing on the sample, passes through a set of objective (forming and enlarging) and ocular (enlarging) lenses. In addition to enlarging the image of an object, the microscope serves to increase the resolving power of the human eye (0.1 - 0.2 mm). Resolving power is the ability to distinguish two points very close to one another. Optical microscopes have a resolution limit in the order of 0.2 *μm*, that is, the lenses of these microscopes can show two distinct points if they are distant of at least 0.2 *μm* (MURPHY, 2001).

In this study, mirror-like polished samples with a surface roughness of 1 *μm* were analyzed using a ZEISS model optical microscope to quantify the volume fraction of the amorphous phase (V_f) of all as-cast 105 Vit alloy samples, as well as the heat-affected zones of all welded samples. Transverse-section images of the welded samples were prepared and phase quantification accomplished using the ZEISS AxioVs40 V4.8.2.0 software according to ASTM E1245-03 (2016).

3.2.4 Scanning Electron Microscopy

Scanning electron microscopy is used whenever there is a need for very powerful magnification of a specimen's topography. With a scanning electron microscope, it is possible to achieve magnifications about 300,000 times. SEM inspection is often used in the analysis of cracks and fracture surfaces, bond failures, physical defects, phase determination, quantification and distribution among other useful utilities.

A beam of electrons is focused on a small spot volume of the specimen, resulting in energy transfer to the spot. The electrons bombarding the topography of the specimen are known as primary electrons which remove electrons from the specimen itself. These dislodged electrons are known as secondary electrons. They are attracted and collected by a positively biased grid or detector, and then translated into a signal.

To produce the SEM image, the electron beam is scanned across the area of interest, producing many such signals. These signals are then amplified, analyzed, and translated into images of the topography being inspected.

3.2.5 Thermal Imaging

Infrared thermography, or thermal imaging, is the non-contact method that detects radiation in the long-infrared range of the electromagnetic spectrum to produce images of that radiation, called thermogramms. All matter above the absolute zero temperature emit infrared radiation, which makes it possible to detect variation of a body's temperature using special infrared video cameras.

During resistance upset welding, the heat distribution around the interface of specimens S3, S4, S5 and S6 were measured using a FLIR T650sc thermal imaging camera, according to Shin et al. (2005), to record peak temperature (T_p), heating and cooling rates and, heat distribution in the samples interface. From the images analysis, the heating rate was determined from room temperature up to peak temperature (T_p), and cooling rate determined from T_p to T_g.

3.2.6 Microhardness Testing

Microindentation testing is an outstanding way to investigate the elasto-plastic behavior of materials. It allows to gain insight into a materials micromechanisms of plastic deformation and their response to multiaxial loading (RAMAMURTY, 2005). Vickers microhardness was measured using a BUEHLER VH1102 model at the joining interfaces and positions -1 and +1 mm from the interface with a 2 N force. At each position, 6 microindentations were performed and the mean, standard deviation and statistical error within a 90% confidence interval calculated.

3.3 Welding Procedure

A partial factorial design with two factors (welding current and welding time), 3 levels for welding current, 2 levels for welding time, experiment was designed for the welding procedure. An extra weld with higher welding energy was produced for comparison. For welding current, the levels were 26, 28 and 30% of the nominal electrical current of the welding machine. For welding time (t), 1.16 and, 1.25 seconds were used.

The welding pressure was setup at 1 MPa. A resistance upset welder, 20 kVA AC, 60 Hz was used. The bonding surfaces were mechanically grinded up to 600-mesh using SiC abrasive paper to improve contact resistance. Then it was cleaned by an ultrasonic treatment in acetone for 300 s. All welds were done under an argon flux of 10 l/min to minimize surface oxidation.

The electrical data during the welding process was collected using a MINIPA oscilloscope. An oscilloscope probe and a Rogowski coil (FURLANETTO, 2010) were coupled to the electrodes and the machine secondary conductor, respectively. From the electrical data, the thermal energy was calculated according to equation 2.9. From this point on, samples are to be labeled (S1, S2, S3, S4, S5, S6 and, S7), according to their thermal energies as shown in table 3.2.

Table 3.2 Experimental design, sample labels and resulting thermal energies from the welding operation.

	Level						
Welding current (%)	26		28		30		35
Welding time (s)	1.16	1.25	1.16	1.25	1.16	1.25	1.25
Sample label	S1	S2	S3	S4	S5	S6	S7
Thermal energy (J)	3157	3700	3770	4350	5750	5960	> 10000

Source: Authors of this thesis (2017).

4. RESULTS AND DISCUSSION

4.1 Base Metal Characterization

4.1.1 Differential Scanning Calorimetry

Figure 4.1 presents the DSC thermogram of the as-cast VIT 105 BMG at a 0.33 K/s heating rate. It is evident the T_g, T_x and the T_l at 394, 460 and 825 ºC, respectively. These results are in good agreement with the values described by Hofmann et al. (2016). From the results, the width of ΔT_x was computed, according to Eq. 2.2, showing the good glass stability of this alloy composition. It is important to know the value of ΔT_x when welding BMGs since in this temperature interval they can be easily deformed without devitrification occurring. The results from the DSC curves are summarized in table 4.1.

Fig. 4.1 – Differential scanning calorimetry curve of the as-cast VIT 105 BMG at a 0.33 K/s heating rate showing T_g, T_x and T_l.

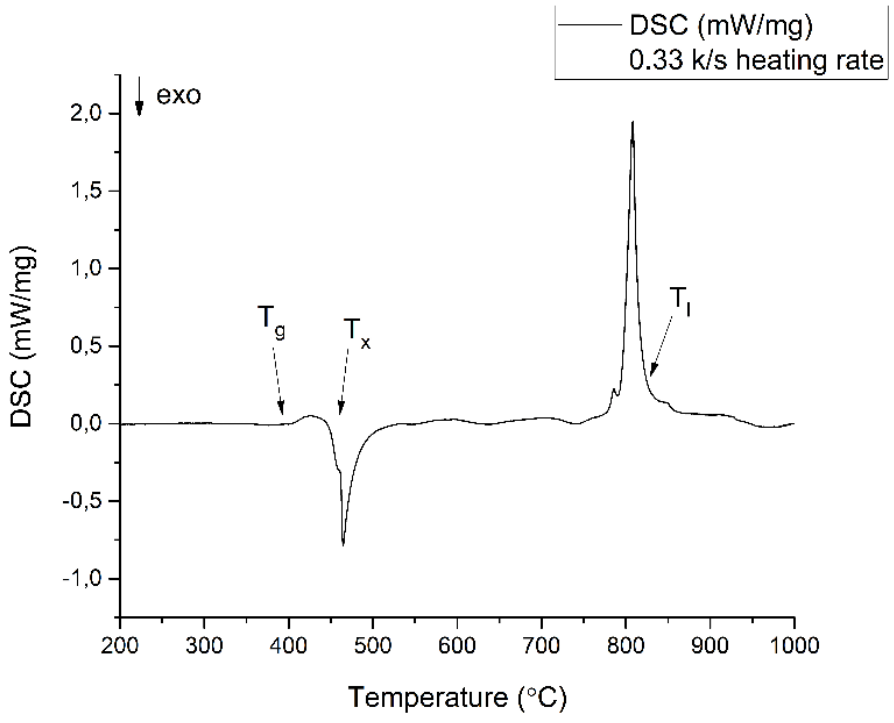

Source: Authors of this Thesis (2017).

Table 4.1 – DSC results for the as-cast VIT 105 alloy.

T_g (ºC)	T_x (ºC)	T_l (ºC)	ΔT_x (ºC)
394	460	825	66

Source: Authors of this thesis (2017).

4.1.2 X-ray Diffraction Pattern

Figure 4.2 presents the diffraction pattern of the as-cast alloy. Only broad and diffuse peaks around 2θ (38° and 65°) are evident. These broad peaks correspond to the medium and short-range atomic arrangements of the glassy phase. The XRD technique has no sensibility to detect crystal structures with volume fraction below 3-5 %, therefore, no crystalline peaks are revealed, despite minor crystalline fraction was detected by OM.

Fig. 4.2 – X-ray diffraction pattern of the as-cast VIT 105 base metal.

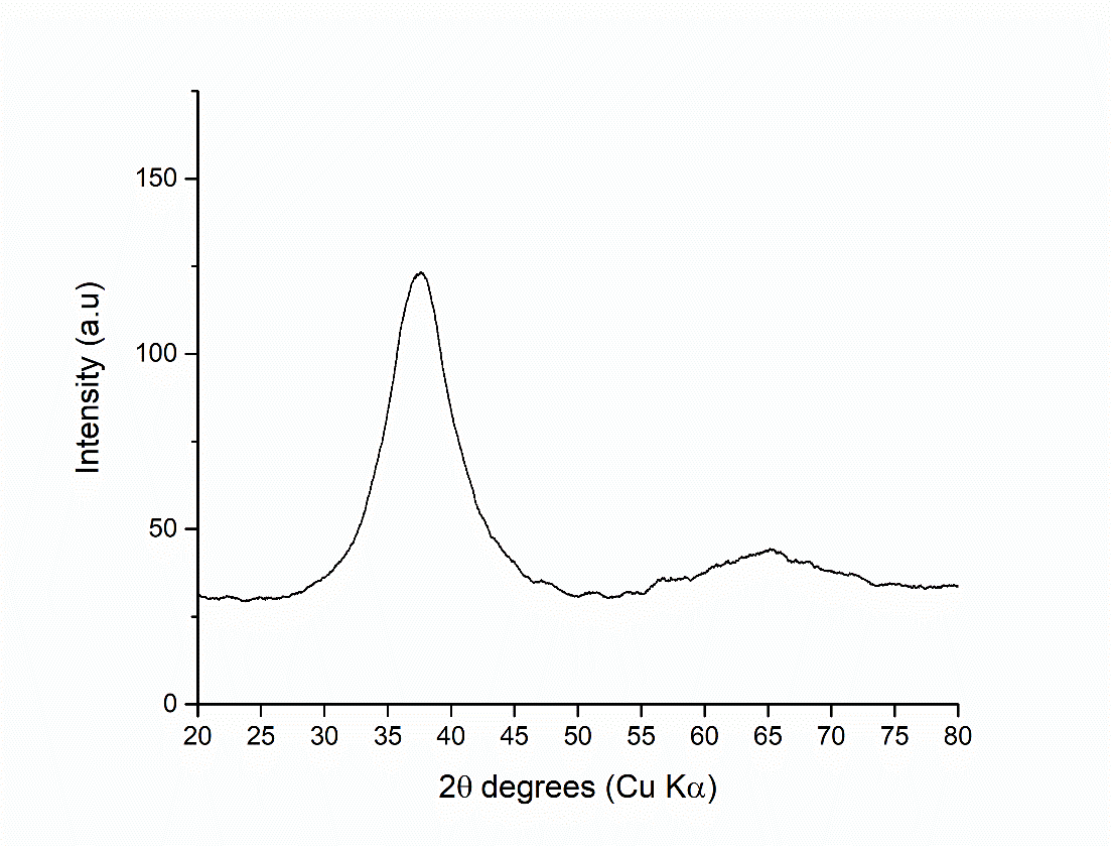

Source: Authors of this thesis (2017).

4.1.3 Microscopy Analysis

The amorphous phase volume fraction (V_f) of all as-cast samples used in the welding experiment are shown in Figure 4.3. All samples have V_f above 98% proving the good GFA of the alloy composition and the effectiveness of the casting method. The mean V_f of the samples produced was 99.2 ±0.36% for a 90% confidence interval.

Figure 4.3 – The amorphous phase volume fraction of the as-cast VIT 105 samples before welding.

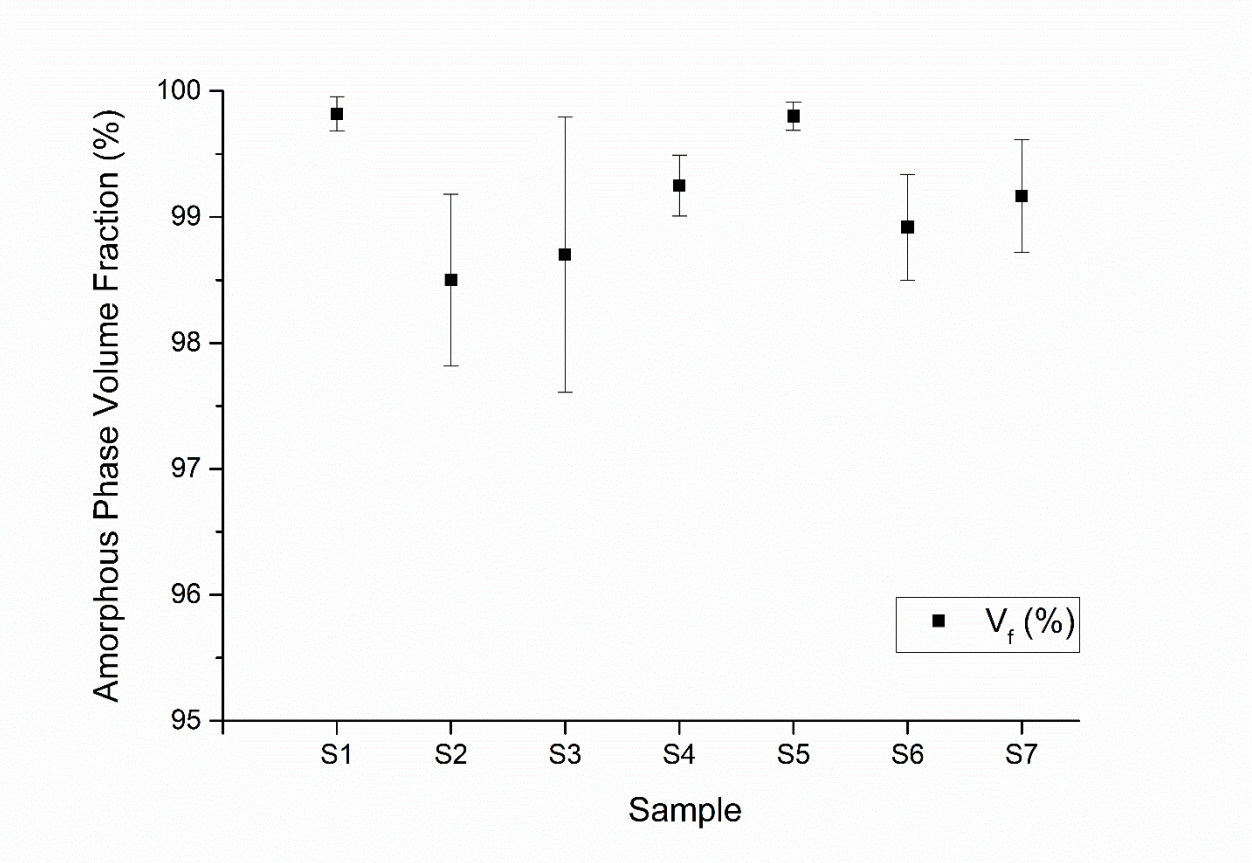

Source: Authors of this thesis (2017).

4.2 Heat-Affected Zone Characterization

Figure 4.4 shows the outer appearance of welded samples S3 and S6. One may notice the different shape of the protrusions formed during the UW process in the HAZ with the increase in thermal energies. For sample S6, the higher deformation is attributed to excessive viscous flow in the supercooled liquid state. In addition, it is clear to observe

the greater surface oxidation with the increase in thermal energy. This is due to the diffusion temperature dependence of oxygen in the metal surface.

Fig. 4.4 – Outer appearance of samples S3 (3770 J) and S6 (5960 J) after the resistance upset welding process with different parameters setup.

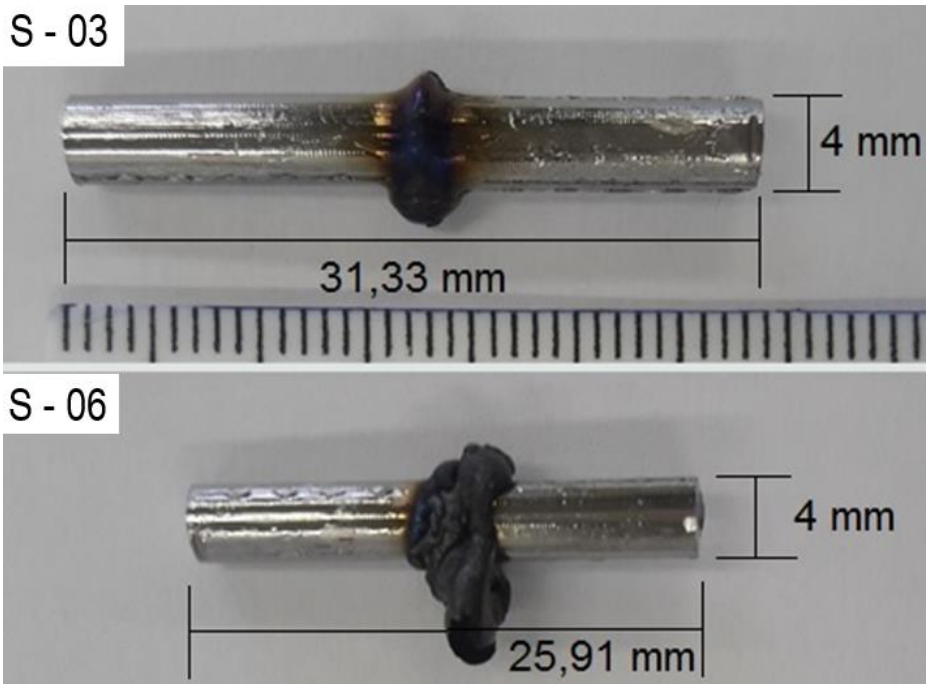

Source: Authors of this thesis (2017).

4.2.1 X-ray Diffraction Patterns

Figure 4.5 shows the diffraction patterns of samples, S3, S5, and S7. From the diffraction patterns, it is distinct to observe the evolution of crystallization in the HAZ with the increase in thermal energy. For sample S3, only a broad and diffuse peak is seen confirming the amorphous nature of the joint. For sample S5, diffraction peaks are of the NiZr2 “big cube” phase, which are in accordance with the results found by Kuroda et al. (2009), for resistance welding of a Zr-based BMG. In addition to crystalline peaks, a discrete diffuse and broad peak is yet present representing the amorphous phase. For sample S7, peaks of crystalline compounds are evident for the CuZr2 tetragonal phase. According to Wang et al. (2000), “despite the complexity of different crystallization paths, the main final crystallized product in the Zr-based BMGs is Zr2Cu”. Baricco et al. (2001)

have noticed a similar crystallization behavior during thermal annealing of a Zr-based BMG at different temperatures. For lower temperatures, the NiZr2 “big cube” phase precipitates while annealing at higher temperatures the CuZr2 phase forms. For sample S7, the amorphous diffuse peak is barely noticed. It is a strong evidence that for the highest thermal energy, the welding process occurred beyond the optimum ΔT_x interval and complete crystallization of the HAZ occurred.

Figure 4.5. XRD patterns of the HAZ for samples, S3, S5, and S7. The XRD patterns represent a 0.6 mm X-ray beam line at the weld interface.

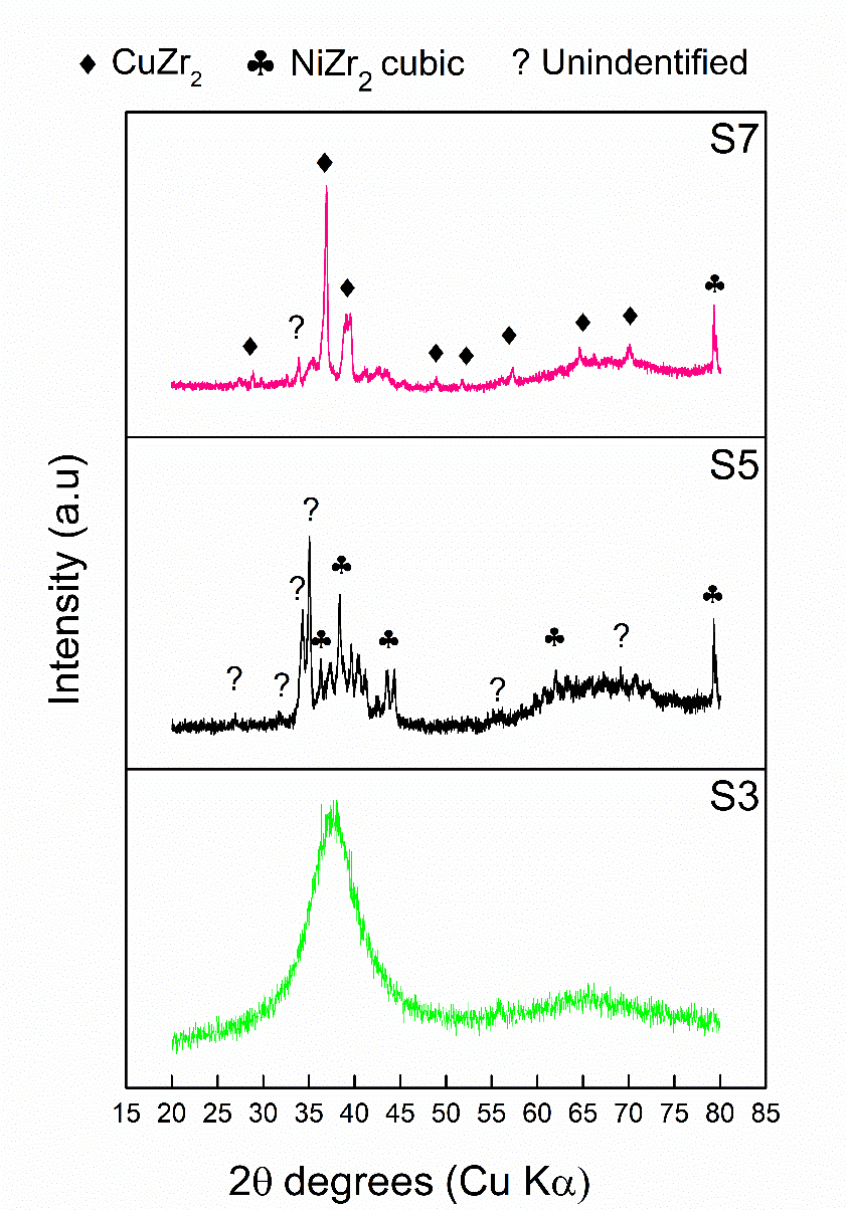

Source: Authors of this thesis (2017).

4.2.2 Thermal Imaging Data

The thermal data acquired using a FLIR T650sc camera, during the welding operation of samples S3, S4, S5 and S6 is provided in table 4.2. Peak temperature (T_p), time interval above T_x, heating and cooling rates are described. For samples S3 and S4, the peak temperatures did not rise above the T_x measured by DSC at a 0.33 k/s (table 4.1). Notwithstanding, sample S4 revealed a very narrow crystallization line in the HAZ. It is known from the literature that the heating rate affect both T_g and T_x. “The crystallization process is largely retarded by a delay of the diffusion at a high heating rate” (ICHITSUBO et al., 2005). This is reasonable to explain why S4 experienced crystallization in the HAZ while S3 retained its amorphous structure. Furthermore, the cooling rate for sample S4 was lower compared to others. For samples S5 and S6 the time interval that samples remained above T_x was sufficient to provide the energy needed for atom diffusion and the formation of crystalline compounds. Ultimately, the formation of brittle crystalline phases in the HAZ cause the joints to fail. The crystalline phases formed during the devitrification of $Zr_{52.5}Cu_{17.9}Ni_{14.6}Al_{10}Ti_5$ BMG are very brittle (SZÉKELY et al., 2002). Cooling-induced thermal stresses potentially lead to the nucleation and growth of cracks that propagate within the brittle crystalline network and terminate in the amorphous matrix (KOSIBA and PAULY, 2017). Figure 4.6 shows the thermograph of sample S3 at the peak temperature.

Table 4.2. Thermal data acquired using a thermal imaging camera during the UW process for S3, S4, S5 and S6 samples.

Sample	Tp (°C)	Time above T_x (ms)	Heating rate (°C/s)	Cooling rate (°C/s)
S3	456.3	0	336.7	55.6
S4	422.8	0	183.2	37.0
S5	492.0	530	314.5	73.7
S6	475.2	770	215.5	52.5

Source: Authors of this thesis (2017).

Figure 4.6 – Thermal image of S3 during the resistance upset welding process.

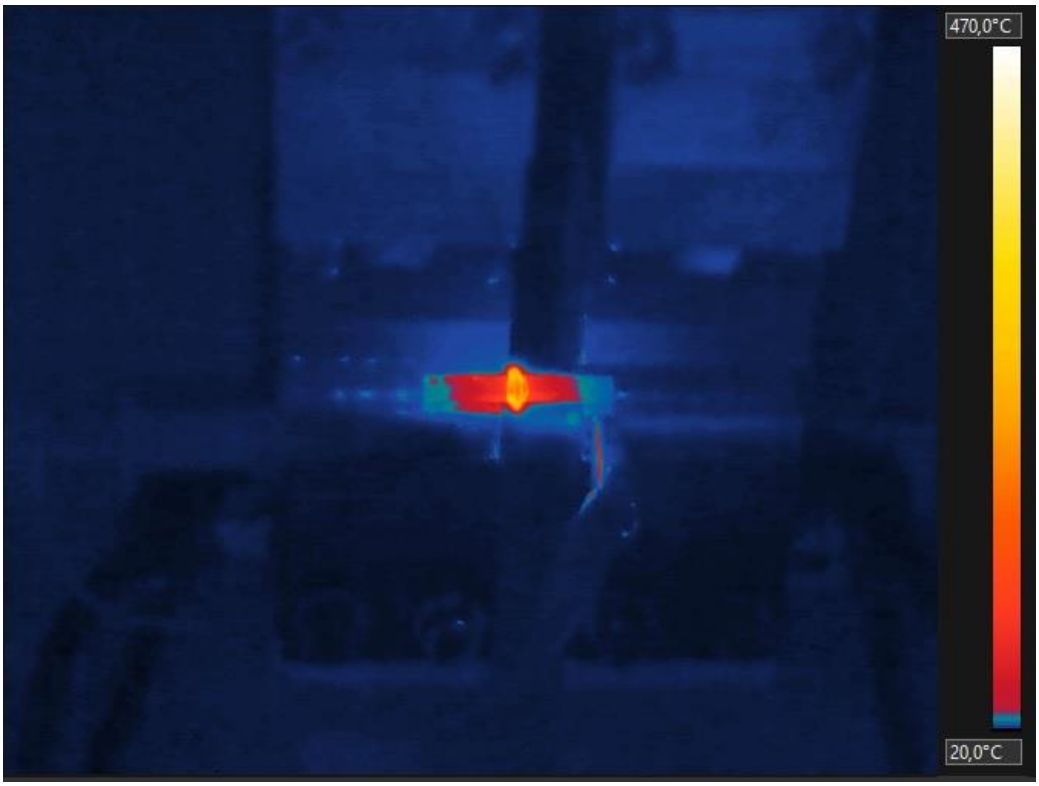

Source: Authors of this thesis (2017).

4.2.3 Amorphous Phase Volume Fraction

The results from the V_f at different positions in the welded joints (Fig. 4.7) corroborate the previous results. For samples with lower welding energies (S1 and S3) no detectable changes in the V_f at the interface (0 mm) and positions -10, -5, 5 and 10 mm are observed, confirming that the welding process did not alter the amorphous structure of the base metal. One may want to compare the V_f prior to the welding process for all samples in Fig. 4.3. With increase in thermal energy, the V_f decreases linearly in the welded zone approaching 0% at the joining interface for the sample with the highest welding energy (S7). Figure 4.8 shows an optical microscopy image of the weld interface for sample S5. It is possible to see the crystalline compounds formed in the HAZ during the welding process.

Figure 4.7 – The amorphous phase volume fraction of samples S1, S3, S4, S5 and S7 after the resistance upset welding process. The joining interface stands for position 0 mm.

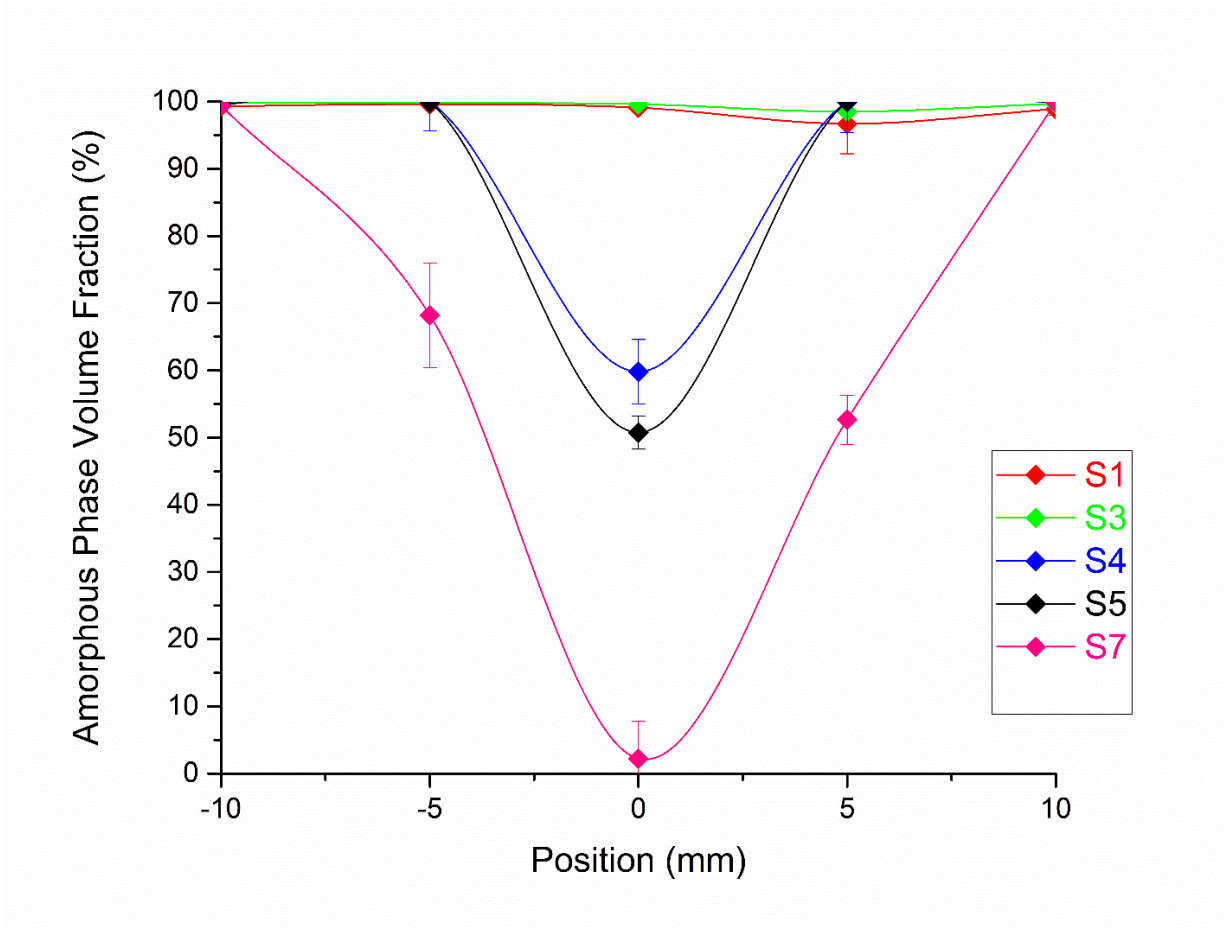

Source: Authors of this thesis (2017).

Figure 4.8 –Interfacial zone of S5 showing the devitrification of the amorphous phase during the UW process (OM).

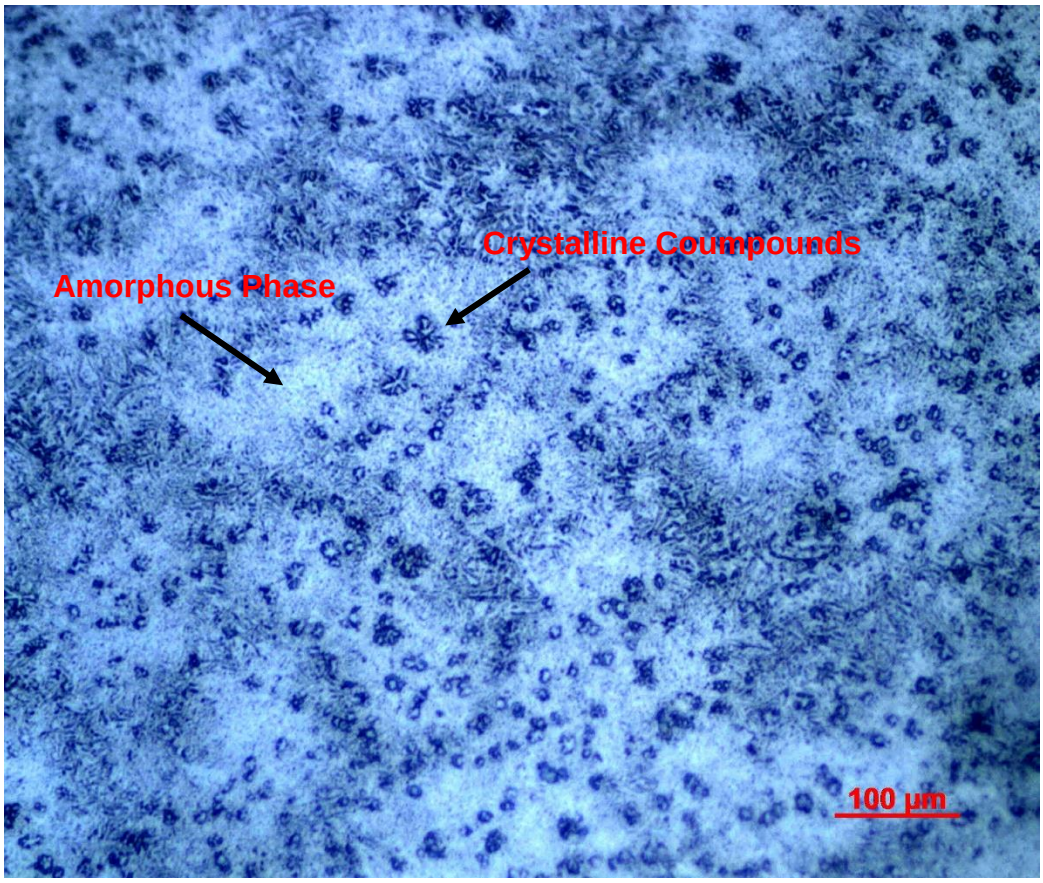

Source: Authors of this thesis (2017).

4.2.4 Scanning Electron Microscopy Analysis

At this point, it is important to emphasize that for sample S1, despite that no changes to the base metal microstructure occurred, only partial bonding of the interface was achieved. This can be seen in the SEM image of the interfacial zone of sample S1 (Fig. 4.9a). It is worth pointing out that the interface acts as a preferential site for corrosion during etching. Nevertheless, an obvious lack of joining in the interface can be observed. The microstructure of the interfacial zone of sample S5 is shown in Figure 4.9b. One may observe the complete crystallization of the interfacial zone. An interesting feature is that the welding energy responsible to produce a sound HAZ with no detectable crystallization (S3) is somewhat close to the energies of samples that show lack of joining and an amorphous HAZ (S1) to those samples (S4, S5, S6) that crystalline compounds formed

in the HAZ. This demonstrates that the welding parameters have a very narrow range for setup, even though the supercooled liquid window is around 60 °C.

Figure 4.9 – (a) Secondary electron mode (SE) SEM image of sample S1 evidencing a lack of joining in the interface. (b) Interfacial zone of sample S5 where crystallization occurred during the welding procedure (SE SEM image).

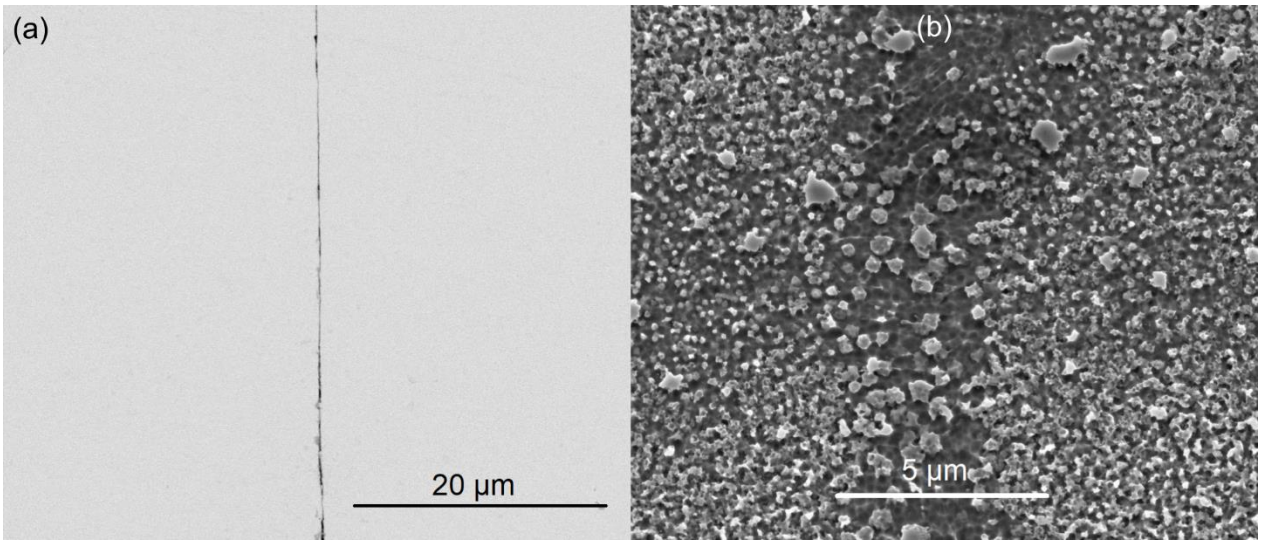

Source: Authors of this thesis (2017).

Figure 4.10 shows a SE mode SEM image of sample 3. It is possible to see a sound weld and no indication of crystalline compounds within the amorphous phase matrix.

Figure 4.10 – SE SEM image of S3 showing a sound joining in the interface of a Zr-based BMG.

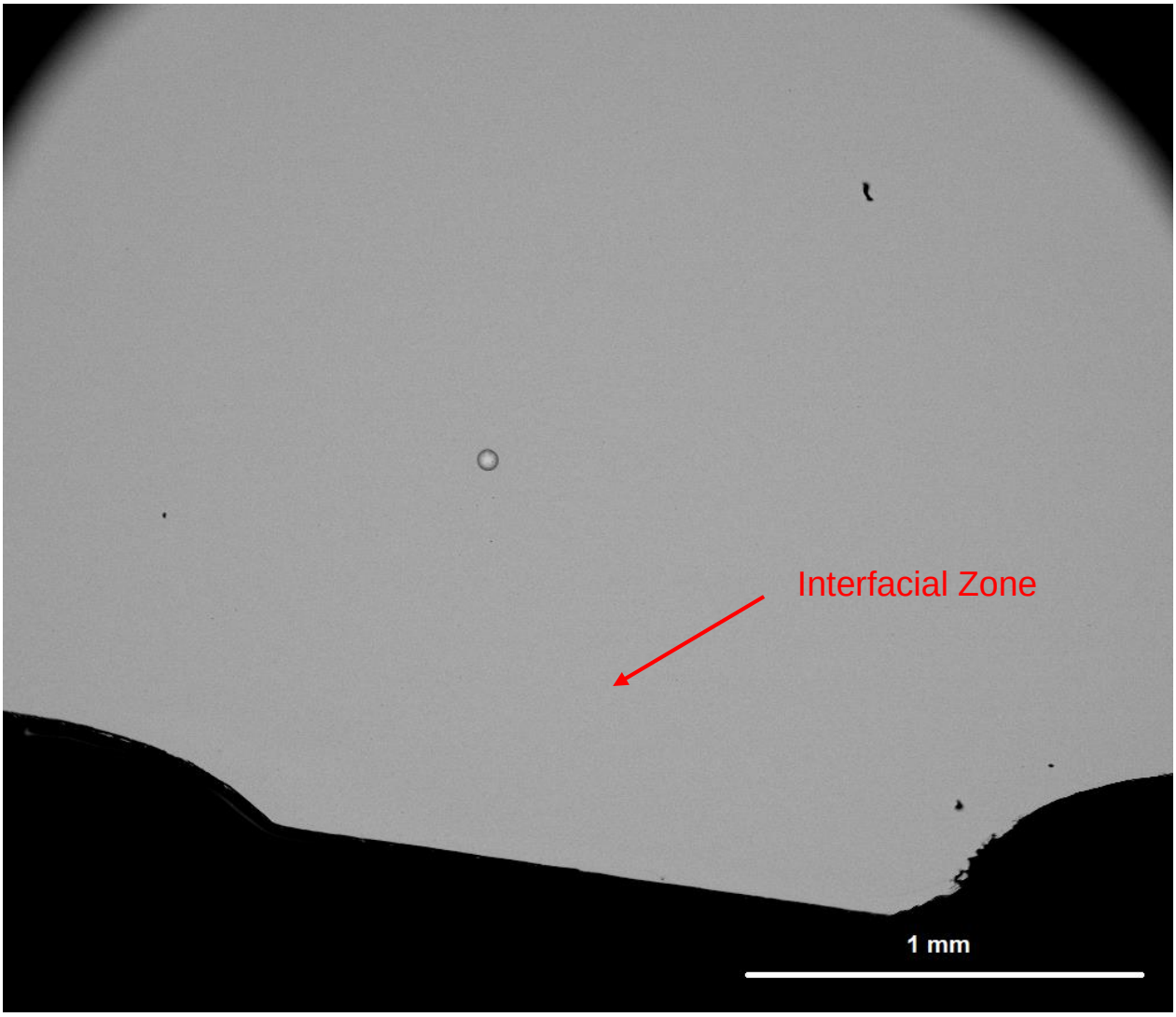

Source: Authors of this thesis (2017).

4.2.5 Vickers Microhardness

To assess the mechanical response of the welded samples, Vickers microhardness was performed along the HAZ of welded samples. As can be seen in Fig. 4.11, the hardness of samples where no crystallization in the interface was detected (S1 and S3) remains relatively, within the measured error, equal to the non-heat-affected zone (positions -1, 1 mm). A small increment in hardness at the interface position may be due to the formation of nanocrystals with a typical size of 5 to 20 nm. This phenomenon has

been previously reported after annealing of Zr-based BMGs (FAN and INOUE, 2000). Crystals with this grain size were not detected neither by XRD nor by SEM analysis, for samples S1, S2, and S3. With the increase in welding energy and a large decrease in the V_f (Fig. 6), the hardness in the HAZ increases dramatically. The crystalline compounds formed during the devitrification of Zr-based BMGs have superior hardness compared to the amorphous phase, however, with a substantial loss in ductility (SZÉKELY et al., 2002).

Figure 4.11 – Microhardness profile along the heat-affected zone of the welded samples with different thermal energies. Interface stands for position 0 mm.

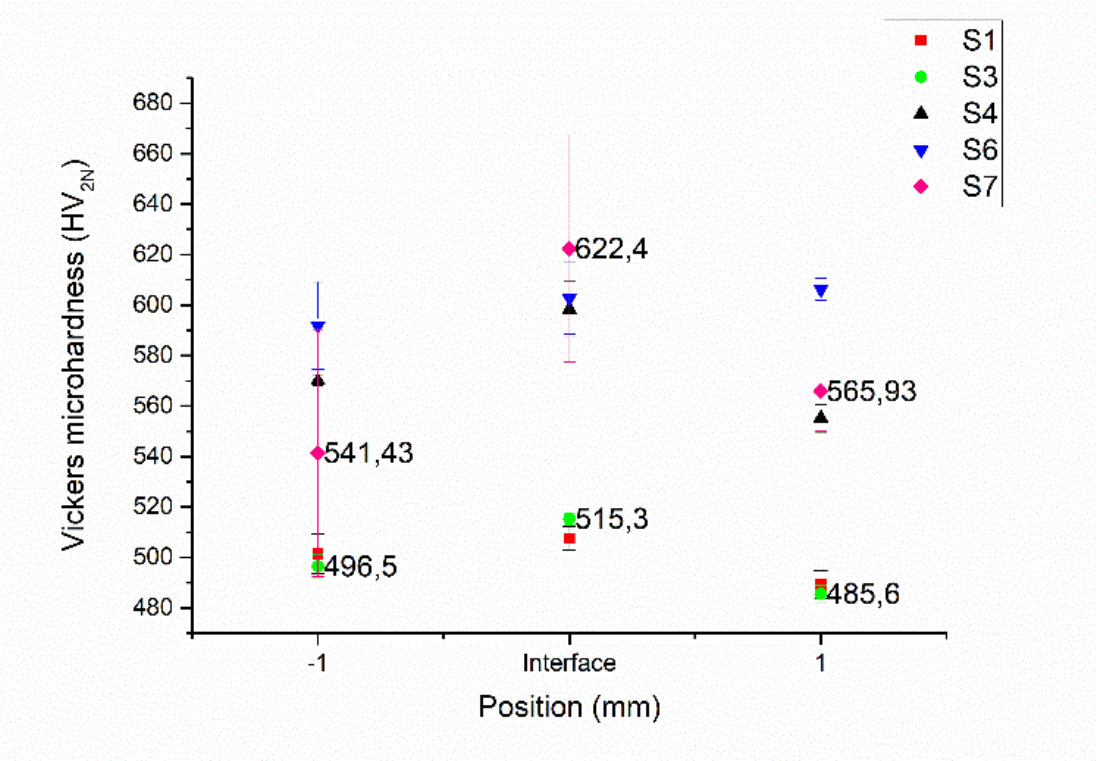

Source: Authors of this thesis (2017).

5. CONCLUSION

We were successful to join, by the resistance upset technology, 4 mm rods of a Zr-based bulk metallic glass. The interfacial weld zone did not show signs of crystallization and the hardness profile measured along the HAZ was the same as for the base metal.

The increase in thermal energy has a detrimental effect to HAZ leading to partial or full crystallization, which eventually leads the joints to fail.

Although the alloy has a large supercooled window (ΔT_x) of approximately 60 °C the welding setup parameters range is very narrow.

6. REFERENCES

ASHBY, M.; GREER, A. Metallic Glasses as Structural Materials. **Scripta Materialia,** v. 54, n. 3, p.321-326, Feb. 2006. Elsevier BV.

ASTM E1245-03, 2016. **Standard practice for determining the inclusion or second-phase constituent content of metals by automatic image analysis**. ASTM International, West Conshohocken.

BARICCO, M. et al. “Big cube” Phase Formation in Zr-based Metallic Glasses. **Materials Science And Engineering: A,** v. 304-306, pp.305-310, 2001. Elsevier BV.

BLEICHER, Lucas; SASAKI, José Marcos. **Introdução a Difração de Raios-X em Cristais.** Natal: Universidade Federal do Rio Grande do Norte, 2000. 20 pp.

BRITO, Pedro Paiva. **Influência da Força na Soldagem de Topo por Resistência do Aço Inoxidável AISI 409.** 2007. 104 f. Dissertação (Mestrado) - Curso de Programa de Pós-Graduação em Engenharia Mecânica, Pontifícia Universidade Católica de Minas Gerais, Belo Horizonte, 2007.

CHEN, H. S.; TURNBULL, D. Thermal Evidence of a Glass Transition in Gold-Silicon-Germanium Alloy. **Applied Physics Letters,** v. 10, n. 10, pp.284-286, 1967. AIP Publishing.

DEMETRIOU, Marios D. et al. A damage-tolerant glass. **Nature Materials,** v. 10, n. 2, pp.123-128, Jan. 2011. Springer Nature.

DÉO, L.P.; OLIVEIRA, M.F. de. Accuracy of a selection criterion for glass forming ability in the Ni–Nb–Zr system. **Journal of Alloys and Compounds,** v. 615, pp.23-28, dez. 2014. Elsevier BV.

DU, Xinghao et al. Designing Ductile Zr-Based Bulk Metallic Glasses with Phase Separated Microstructure. **Advanced Engineering Materials,** v. 11, n. 5, pp.387-391, May 2009. Wiley-Blackwell.

EGAMI, Takeshi; IWASHITA, Takuya; DMOWSKI, Wojciech. Mechanical Properties of Metallic Glasses. **Metals,** v. 3, n. 1, pp.77-113, Jan. 2013. MDPI AG.

ElectronicsTutorials. **Transformer Basics**. Available at: http://www.electronics-tutorials.ws/transformer/transformer-basics.html. Accessed on August 5th 2016.

FAN, Cang; INOUE, Akihisa. Ti-Containing Zr Based Bulk Amorphous/Nanocrystalline Composite Alloys. **Materials Transactions,** v. 41, n. 11, pp.1467-1470, 2000. Japan Institute of Metals.

FUJIWARA, K. et al. Weldability of $Zr_{50}Cu_{30}Al_{10}Ni_{10}$ bulk glassy alloy by small-scale resistance spot welding. **Materials Science and Engineering: A,** v. 498, n. 1-2, pp.302-307, Dec. 2008. Elsevier BV.

FURLANETTO, Valdir. **Desenvolvimento e Instrumentação de um Cabeçote de Soldagem por Ponto por Resistência Elétrica para Aplicação em Condições Industriais.** 2010. 280 f. Tese (Doutorado) - Curso de Engenharia Mecânica, Universidade de São Paulo, São Paulo, 2010.

GAITHER, C. C.; CAVAZOS-GAITHER, Alma. **Scientifically Speaking:** A Dictionary of Quotations. 2. ed. Boca Raton: Crc Press, 2000. 482 pp.

GREER, A. L.; RUTHERFORD, K. L.; HUTCHINGS, I. M. Wear Resistance of Amorphous Alloys and Related Materials. **International Materials Reviews,** v. 47, n. 2, pp.87-112, Apr. 2002.

GU, X. J. et al. Ductility Improvement of Amorphous Steels: Roles of Shear Modulus and Electronic Structure. **Acta Materialia,** v. 56, n. 1, pp.88-94, Jan. 2008. Elsevier BV.

HOFFMAN, D. C. et al. **Joining and Assembly of Bulk Metallic Glass Composites through Capacitive Discharge.** . Ed: NASA Tech Brief, 2012. 2 pp.

HOFMANN, Douglas C. et al. Castable Bulk Metallic Glass Strain Wave Gears: Towards Decreasing the Cost of High-Performance Robotics. **Scientific Reports,** v. 6, n. 1, pp.1-11, 24 Nov. 2016. Springer Nature.

ICHITSUBO, Tetsu et al. Local Structure and Glass Transition in Zr-Based Binary Amorphous Alloys. **Materials Transactions,** v. 46, n. 10, pp.2282-2286, 2005. Japan Institute of Metals.

INOUE, A. et al. Cobalt-Based Bulk Glassy Alloy with Ultrahigh Strength and Soft Magnetic Properties. **Nature Materials,** v. 2, n. 10, pp.661-663, Sep. 2003. Springer Nature.

INOUE, A.; TAKEUCHI, A. Recent Development and Application Products of Bulk Glassy Alloys. **Acta Materialia,** v. 59, n. 6, pp.2243-2267, Apr. 2011. Elsevier BV.

INOUE, Akihisa et al. Enhanced Shot Peening Effect for Steels by Using Fe-based Glassy Alloy Shots. **Materials Transactions,** v. 44, n. 11, pp.2391-2395, Oct. 2003.

INOUE, Akihisa. High Strength Bulk Amorphous Alloys with Low Critical Cooling Rates (Overview). **Materials Transactions,** v. 36, n. 7, pp.866-875, Jul. 1995.

INOUE, Akihisa. Stabilization of Metallic Supercooled Liquid and Bulk Amorphous Alloys. **Acta Materialia,** v. 48, n. 1, pp.279-306, Jan. 2000. Elsevier BV.

INOUE, Akihisa; TAKEUCHI, Akira. Recent Progress in Bulk Glassy Alloys. **Materials Transactions,** v. 43, n. 8, pp.1892-1906, Apr. 2002.

INOUE, Akihisa; TAKEUCHI, Akira. Recent Progress in Bulk Glassy, Nanoquasicrystalline and Nanocrystalline Alloys. **Materials Science and Engineering: A,** v. 375-377, pp.16-30, Jul. 2004. Elsevier BV.

ISHIDA, Mamoru et al. Wear Resistivity of Super-Precision Microgear Made of Ni-based Metallic Glass. **Materials Science and Engineering: A,** v. 449-451, pp.149-154, Mar. 2007.

JOHNSON, W. L. Bulk Glass-Forming Metallic Alloys: Science and Technology. **MRS Bulletin,** v. 24, n. 10, p.42-56, Oct. 1999. Cambridge University Press.

JOHNSON, William L. Is Metallic Glass Poised to Come of Age? **Nature Materials,** v. 14, n. 6, pp.553-555, May 20, 2015. Nature Publishing Group.

KANNE Jr W. R. Solid-State Resistance Upset Welding: A Process with Unique Advantages for Advanced Materials**. Advanced Joining Technologies for New Materials II**, Cocoa Beach, Florida, 1994.

KAWAMURA, Y. et al. Superplastic deformation of $Zr_{55}Ni_{10}Cu_{30}AL_5$ metallic glass. **Scripta Materialia,** v. 37, n. 4, p.431-436, Ago. 1997. Elsevier BV.

KAWAMURA, Y. et al. Workability of the supercooled liquid in the $Zr_{65}Al_{10}Ni_{10}Cu_{15}$ bulk metallic glass. **Acta Materialia,** v. 46, n. 1, p.253-263, Dec. 1998. Elsevier BV.

KAWAMURA, Y. Liquid Phase and Supercooled Liquid Phase Welding of Bulk Metallic Glasses. **Materials Science and Engineering: A,** v. 375-377, pp.112-119, Jul. 2004. Elsevier BV.

KAWAMURA, Y.; KAGAO, S.; OHNO, Y. Metallurgical Bonding of Bulk Metallic Glasses. **Materials Transactions,** v. 04, n. 42, pp.717-719, Mar. 14, 2001.

KEARNS, W. H. (Ed.). **AWS Welding Handbook:** Resistance and Solid-State Welding and other Joining Processes. 7. ed. Miami: American Welding Society, 1980. 461 pp.

KERSTENS, N. F. H. **Investigation and Control of Factors Influencing Resistance Upset Butt Welding.** 2010. 190 f. Tese (Doutorado) - Materiaal Ingenieur, Technische Universiteit Delft, Delft, 2009.

KIM, W.J.; MA, D.S.; JEONG, H.G. Superplastic flow in a $Zr_{65}Al_{10}Ni_{10}Cu_{15}$ metallic glass crystallized during deformation in a supercooled liquid region. **Scripta Materialia,** v. 49, n. 11, p.1067-1073, Dec. 2003. Elsevier BV.

KLEMENT, W.; WILLENS, R. H.; DUWEZ, Pol. Non-crystalline Structure in Solidified Gold–Silicon Alloys. **Nature,** v. 187, n. 4740, pp.869-870, Sept. 3, 1960. Springer Nature.

KOSIBA, K.; PAULY, S. Inductive Flash-Annealing of Bulk Metallic Glasses. **Scientific Reports,** v. 7, n. 1, pp.1-11, 2017. Springer Nature.

KURODA, Toshio et al. Microstructure of Bonding Interface for Resistance Welding of Zr-Based Metallic Glass Sheets. **Materials Transactions,** v. 50, n. 6, pp.1259-1262, 2009. Japan Institute of Metals.

KUO, Pei-Hung et al. Bulk-metallic glasses joining in a supercooled-liquid zone. **Materials Chemistry and Physics,** v. 120, n. 2-3, pp.532-536, 2010. Elsevier BV.

LEWANDOWSKI, J. J.; WANG, W. H.; GREER, A. L. Intrinsic Plasticity or Brittleness of Metallic Glasses. **Philosophical Magazine Letters,** v. 85, n. 2, p.77-87, Feb. 2005. Informa UK Limited.

LI, H.; ZHENG, Y. Recent Advances in Bulk Metallic Glasses for Biomedical Applications. **Acta Biomaterialia,** v. 36, pp.1-20, May 2016. Elsevier BV.

LIU, L.; WU, Z.F.; ZHANG, J. Crystallization kinetics of $Zr_{55}Cu_{30}Al_{10}Ni_5$ bulk amorphous alloy. **Journal of Alloys and Compounds,** v. 339, n. 1-2, pp.90-95, Jun. 2002.

MAKHANLALL, D. et al. Joining of Ti-based bulk metallic glasses using resistance spot welding technology. **Journal of Materials Processing Technology,** v. 212, n. 8, pp.1790-1795, Ago. 2012. Elsevier BV.

MATTERN, N. et al. Short-range Order of Cu–Zr Metallic Glasses. **Journal of Alloys and Compounds,** v. 485, n. 1-2, pp.163-169, Oct. 2009. Elsevier BV.

MILLER, Michael; LIAW, Peter (Ed.). **Bulk Metallic Glasses:** An Overview. Springer Science and Business Media, 2007. 249 pp.

MURPHY, Douglas B. **Fundamentals on light microscopy and electronic imaging.** New York: Wiley-Liss, 2001. 357 pp.

OLIVEIRA, M. F. de et al. Electromechanical engraving and writing on bulk metallic glasses. **Applied Physics Letters,** v. 81, n. 9, pp.1606-1608, Ago. 2002. AIP Publishing.

PEREIRA, Flávio S. **Desenvolvimento de um Processo para a Produção de Peças Metálicas Vítreas.** 2009. 80 f. Dissertação (Mestrado) - Curso de Programa de Pós-Graduação em Interunidades Ciências e Engenharia de Materiais, Universidade de São Paulo, São Carlos, 2009.

PODRžAJ, P. et al. Overview of Resistance Spot Welding Control. **Science and Technology of Welding and Joining,** v. 13, n. 3, pp.215-224, Apr. 2008. Informa UK Limited.

QIN, Fengxiang et al. Ti-Based Bulk Metallic Glasses for Biomedical Applications. In: LASKOVSKI, Anthony N. (Ed.). **Biomedical Engineering:** Trends in Material Science. Rijeka: InTech, 2011. Cap. 11. p. 249-268.

RAMAMURTY, U. et al. Hardness and Plastic Deformation in a Bulk Metallic Glass. **Acta Materialia,** v. 53, n. 3, p.705-717, Feb. 2005. Elsevier BV.

RESISTANCE WELDING MANUFACTURING ALLIANCE (RWMA) (Ed.). **Resistance Welding Manual.** 4. ed. Miami: American Welding Society (AWS), 2003. 503 pp.

SALEM, Meranda. **Control and Power Supply for Resistance Spot Welding (RSW).** 2011. 130 f. Tese (Doutorado) - Curso de Electrical and Computer Engineering, Western University, London, 2011.

SENKARA, J.; ZHANG, H. **Resistance Welding: Fundamentals and Applications**. Boca Raton: CRC Press, 2006.

SHAMLAYE, K. F. et al. Bonding of Mg-base metallic glass through rapid resistive welding. **Materials Science and Technology,** v. 5, n. 8, pp.1-8, Nov. 2012.

SHIN, Hyung-Seop et al. Friction Welding of $Zr_{55}Al_{10}Ni_5Cu_{30}$ Bulk Metallic Glasses. **Materials Transactions,** v. 46, n. 12, pp.2768-2772, 2005. Japan Institute of Metals.

SINGH, Gurjeet; ARORA, Nitin. Design and Development of Micro Upset Welding Setup. **International Journal of Mechanical Engineering and Robotics Research,** v. 2, n. 2, pp.51-58, Apr. 2013.

SONG, Q. et al. An Experimental Study Determines the Electrical Contact Resistance in Resistance Welding. **Welding Journal**, v. 84, n. 5, pp. 73s-76s, May 2005.

SOUZA, Erivelto Luís de et al. Improvement of metallic joint electrical conductivity using a novel conductive paste produced from recycled residues. **Rem: Revista Escola de Minas,** v. 59, n. 2, pp.213-216, Jun. 2006. FapUNIFESP (SciELO).

SPEAKMAN, Scott A. **Basics of X-Ray Powder Diffraction:** Required Training to Become an Independent User in the X-Ray SEF. Available at: <http://prism.mit.edu/xray/>. Accessed: Feb. 6, 2017.

SURYANARAYANA, C.; INOUE, A. (Ed.). **Bulk Metallic Glasses.** Boca Raton: Crc Press, 2010. 548 pp.

SZÉKELY, Ferenc et al. Effects of Crystals on the Mechanical Properties of $Zr_{52.5}Ti_5Cu_{17.9}Ni_{14.6}Al_{10}$ Bulk Metallic Glasses. **Annales de Chimie Science Des Matériaux,** v. 27, n. 5, pp.125-130, 2002. Elsevier BV.

TAKEUCHI, Akira; INOUE, Akihisa. Quantitative Evaluation of Critical Cooling Rate for Metallic Glasses. **Materials Science and Engineering: A,** v. 304-306, pp.446-451, May 2001. Elsevier BV.

TAN, W. et al. A Study of Dynamic Resistance during Small Scale Resistance Spot Welding of Thin Ni Sheets. **Journal of Physics D**: Applied Physics, v. 37, n. 14, pp. 1998-2008, Jun. 30, 2004.

TANG, H. et al. Influence of Welding Machine Mechanical Characteristics on the Resistance Spot Welding Process and Weld Quality. **Welding Journal**, v. 82, pp. 116s-124s, May 2003.

TELFORD, Mark. The Case for Bulk Metallic Glass. **Materials Today,** v. 7, n. 3, pp.36-43, Mar. 2004. Elsevier BV.

UC RUSAL. **The History of Aluminum Industry**. Available at http://www.aluminiumleader.com/history/industry_history/. Accessed on June 21, 2016.

UMETSU, Rie Y.; TU, Rong; GOTO, Takashi. Thermal and Electrical Transport Properties of Zr-Based Bulk Metallic Glassy Alloys with High Glass-Forming Ability. **Materials Transactions,** v. 53, n. 10, pp.1721-1725, 2012. Japan Institute of Metals.

WANG, Gang et al. Resistance spot welding of $Ti_{40}Zr_{25}Ni_3Cu_{12}Be_{20}$ bulk metallic glass: experiments and finite element modeling. **Rare Metals,** v. 36, n. 2, p.123-128, Sep. 2014. Springer Nature.

WANG, J. G. et al. Crystallization and **N**anoindentation Behavior of a bulk Zr–Al–Ti–Cu–Ni Amorphous Alloy. **Journal of Materials Research,** v. 15, n. 03, pp.798-807, 2000. Cambridge University Press.

WANG, W. H.; DONG, C.; SHEK, C. H. Bulk Metallic Glasses. **Materials Science and Engineering,** v. 2, n. 44, pp.45-89, May 10 2004.

YOKOYAMA, Y. et al. Oxygen Embrittlement and Effect of the Addition of Ni Element in a Bulk Amorphous Zr-Cu-Al Alloy. **Materials Transactions,** v. 43, n. 3, pp.571-574, Jan. 2002.

ZHANG, Tao; INOUE, Akihisa. New Bulk Glassy Ni-Based Alloys with High Strength of 3000 MPa. **Materials Transactions,** Sendai, v. 43, n. 04, p.708-711, Feb. 2002. The Japan Institute of Metals.

ZHOU, Kang; CAI, Lilong. An Algorithm for Calculating the RMS Value of the Non-Sinusoidal Current Used in AC Resistance Spot Welding. **Journal of Power Electronics,** v. 15, n. 4, pp.1139-1147, Jul. 2015. The Korean Institute of Power Electronics.